The Astronomical Journal, 161:194 (25pp), 2021 April https://doi.org/10.3847/1538-3881/abe38a

TESS Delivers Five New Hot Giant Planets Orbiting Bright Stars from the Full-frame Images

Joseph E. Rodriguez[1,2], Samuel N. Quinn[2], George Zhou[2], Andrew Vanderburg[3], Louise D. Nielsen[4], Robert A. Wittenmyer[5], Rafael Brahm[6,7], Phillip A. Reed[8], Chelsea X. Huang[9,68], Sydney Vach[2], David R. Ciardi[10], Ryan J. Oelkers[11], Keivan G. Stassun[11,12], Coel Hellier[13], B. Scott Gaudi[14], Jason D. Eastman[2], Karen A. Collins[2], Allyson Bieryla[2], Sam Christian[15], David W. Latham[2], Ilaria Carleo[16,17], Duncan J. Wright[5], Elisabeth Matthews[4], Erica J. Gonzales[18,69], Carl Ziegler[19], Courtney D. Dressing[20], Steve B. Howell[21], Thiam-Guan Tan[22], Justin Wittrock[23], Peter Plavchan[23], Kim K. McLeod[24], David Baker[25], Gavin Wang[26], Don J. Radford[27], Richard P. Schwarz[28], Massimiliano Esposito[29], George R. Ricker[9], Roland K. Vanderspek[9], Sara Seager[9,30,31], Joshua N. Winn[32], Jon M. Jenkins[21], Brett Addison[5], D. R. Anderson[13,33], Thomas Barclay[34,35,36], Thomas G. Beatty[37], Perry Berlind[2], Francois Bouchy[4], Michael Bowen[23], Brendan P. Bowler[38], C. E. Brasseur[39], César Briceño[40], Douglas A. Caldwell[21,41], Michael L. Calkins[2], Scott Cartwright[42], Priyanka Chaturvedi[29], Guillaume Chaverot[4], Sudhish Chimaladinne[43], Jessie L. Christiansen[10], Kevin I. Collins[23], Ian J. M. Crossfield[44], Kevin Eastridge[23], Néstor Espinoza[39], Gilbert A. Esquerdo[2], Dax L. Feliz[11], Tyler Fenske[8], William Fong[9], Tianjun Gan[45], Steven Giacalone[20], Holden Gill[20], Lindsey Gordon[24], A. Granados[24], Nolan Grieves[4], Eike W. Guenther[29], Natalia Guerrero[9], Thomas Henning[46], Christopher E. Henze[21], Katharine Hesse[9], Melissa J. Hobson[7,47], Jonathan Horner[5], David J. James[48], Eric L. N. Jensen[49], Mary Jimenez[23], Andrés Jordán[6,7], Stephen R. Kane[50], John Kielkopf[51], Kingsley Kim[43], Rudolf B. Kuhn[52,53], Natasha Latouf[23], Nicholas M. Law[54], Alan M. Levine[9], Michael B. Lund[10], Andrew W. Mann[54], Shude Mao[45,55], Rachel A. Matson[56], Matthew W. Mengel[5], Jessica Mink[2], Patrick Newman[23], Tanner O'Dwyer[25], Jack Okumura[5], Enric Palle[57,58], Joshua Pepper[59], Elisa V. Quintana[34,36], Paula Sarkis[46], Arjun B. Savel[60], Joshua E. Schlieder[34,36], Chloe Schnaible[25], Avi Shporer[9], Ramotholo Sefako[52], Julia V. Seidel[4], Robert J. Siverd[61], Brett Skinner[25], Manu Stalport[4], Daniel J. Stevens[62,63,70], Caitlin Stibbards[23], C. G. Tinney[64], R. G. West[33,65], Daniel A. Yahalomi[2,66], and Hui Zhang[67]

[1] Department of Physics and Astronomy, Michigan State University, East Lansing, MI 48824, USA; jrod@msu.edu
[2] Center for Astrophysics | Harvard & Smithsonian, 60 Garden St., Cambridge, MA 02138, USA
[3] Department of Astronomy, University of Wisconsin-Madison, Madison, WI 53706, USA
[4] Geneva Observatory, University of Geneva, Chemin des Mailettes 51, 1290 Versoix, Switzerland
[5] Centre for Astrophysics, University of Southern Queensland, West St., Toowoomba, QLD 4350, Australia
[6] Facultad de Ingeniería y Ciencias, Universidad Adolfo Ibáñez, Av. Diagonal las Torres 2640, Peñalolén, Santiago, Chile
[7] Millennium Institute for Astrophysics, Chile
[8] Department of Physical Sciences, Kutztown University, Kutztown, PA 19530, USA
[9] Department of Physics and Kavli Institute for Astrophysics and Space Research, Massachusetts Institute of Technology, Cambridge, MA 02139, USA
[10] Caltech IPAC—NASA Exoplanet Science Institute 1200 E. California Ave., Pasadena, CA 91125, USA
[11] Department of Physics and Astronomy, Vanderbilt University, Nashville, TN 37235, USA
[12] Department of Physics, Fisk University, 1000 17th Ave. North, Nashville, TN 37208, USA
[13] Astrophysics Group, Keele University, Staffordshire ST5 5BG, UK
[14] Department of Astronomy, The Ohio State University, 140 West 18th Ave., Columbus, OH 43210, USA
[15] Liberal Arts and Science Academy, Austin, Texas 78724, USA
[16] Astronomy Department and Van Vleck Observatory, Wesleyan University, Middletown, CT 06459, USA
[17] INAF—Osservatorio Astronomico di Padova, Vicolo dell'Osservatorio 5, I-35122, Padova, Italy
[18] Department of Astronomy and Astrophysics, University of California, Santa Cruz, CA 95064, USA
[19] Dunlap Institute for Astronomy and Astrophysics, University of Toronto, Ontario M5S 3H4, Canada
[20] Department of Astronomy, University of California Berkeley, Berkeley, CA 94720-3411, USA
[21] NASA Ames Research Center, Moffett Field, CA 94035, USA
[22] Perth Exoplanet Survey Telescope, Perth, Australia
[23] George Mason University, 4400 University Drive MS 3F3, Fairfax, VA 22030, USA
[24] Department of Astronomy, Wellesley College, Wellesley, MA 02481, USA
[25] Physics Department, Austin College, 900 North Grand Ave., Sherman TX 75090, USA
[26] Tsinghua International School, Beijing 100084, People's Republic of China
[27] Brierfield Observatory, New South Wales, Australia
[28] Patashnick Voorheesville Observatory, Voorheesville, NY 12186, USA
[29] Thüringer Landessternwarte Tautenburg, Sternwarte 5, D-07778 Tautenburg, Germany
[30] Department of Earth, Atmospheric and Planetary Sciences, Massachusetts Institute of Technology, Cambridge, MA 02139, USA
[31] Department of Aeronautics and Astronautics, MIT, 77 Massachusetts Ave., Cambridge, MA 02139, USA
[32] Department of Astrophysical Sciences, Princeton University, 4 Ivy Ln., Princeton, NJ, 08544, USA
[33] Department of Physics, University of Warwick, Gibbet Hill Rd., Coventry CV4 7AL, UK
[34] Exoplanets and Stellar Astrophysics Laboratory, Code 667, NASA Goddard Space Flight Center, Greenbelt, MD 20771, USA
[35] University of Maryland, Baltimore County, 1000 Hilltop Cir., Baltimore, MD 21250, USA
[36] GSFC Sellers Exoplanet Environments Collaboration, NASA Goddard Space Flight Center, Greenbelt, MD 20771, USA
[37] Department of Astronomy and Steward Observatory, University of Arizona, Tucson, AZ 85721, USA
[38] Department of Astronomy, The University of Texas at Austin, Austin, TX 78712, USA
[39] Space Telescope Science Institute, Baltimore, MD 21218, USA
[40] NOIRLab/Cerro Tololo Inter-American Observatory, Casilla 603, La Serena, Chile
[41] SETI Institute, Mountain View, CA 94043, USA
[42] Proto-Logic Consulting LLC, Washington, DC 20009, USA

[43] Thomas Jefferson High School, 6560 Braddock Rd., Alexandria, VA 22312, USA
[44] Department of Physics and Astronomy, University of Kansas, 1251 Wescoe Hall Dr., Lawrence, KS 66045, USA
[45] Department of Astronomy, Tsinghua University, Beijing 100084, People's Republic of China
[46] Max-Planck-Institut für Astronomie, Königstuhl 17, Heidelberg D-69117, Germany
[47] Instituto de Astrofísica, Facultad de Física, Pontificia Universidad Católica de Chile, Chile
[48] ASTRAVEO LLC, P.O. Box 1668, MA 01931, USA
[49] Department of Physics and Astronomy, Swarthmore College, Swarthmore, PA 19081, USA
[50] Department of Earth and Planetary Sciences, University of California, Riverside, CA 92521, USA
[51] Department of Physics and Astronomy, University of Louisville, Louisville, KY 40292, USA
[52] South African Astronomical Observatory, P.O. Box 9, Observatory, 7935, Cape Town, South Africa
[53] Southern African Large Telescope, P.O. Box 9, Observatory, 7935, Cape Town, South Africa
[54] Department of Physics and Astronomy, University of North Carolina at Chapel Hill, Chapel Hill, NC 27599, USA
[55] National Astronomical Observatories, Chinese Academy of Sciences, 20A Datun Rd., Chaoyang District, Beijing 100012, People's Republic of China
[56] U.S. Naval Observatory, Washington, DC 20392, USA
[57] Instituto de Astrofísica de Canarias (IAC), E-38205 La Laguna, Tenerife, Spain
[58] Departamento de Astrofísica, Universidad de La Laguna (ULL), E-38206 La Laguna, Tenerife, Spain
[59] Department of Physics, Lehigh University, 16 Memorial Dr. East, Bethlehem, PA 18015, USA
[60] Department of Astronomy, University of Maryland, College Park, College Park, MD, USA
[61] Gemini Observatory/NSF's NOIRLab, 670 N. A'ohoku Pl., Hilo, HI 96720, USA
[62] Department of Astronomy & Astrophysics, The Pennsylvania State University, 525 Davey Lab, University Park, PA 16802, USA
[63] Center for Exoplanets and Habitable Worlds, The Pennsylvania State University, 525 Davey Lab, University Park, PA 16802, USA
[64] Exoplanetary Science at UNSW, School of Physics, UNSW Sydney, NSW 2052, Australia
[65] Centre for Exoplanets and Habitability, University of Warwick, Gibbet Hill Rd., Coventry CV4 7AL, UK
[66] Department of Astronomy, Columbia University, 550 West 120th St., New York, NY 10027, USA
[67] School of Astronomy and Space Science, Key Laboratory of Modern Astronomy and Astrophysics in Ministry of Education, Nanjing University, Nanjing 210046, Jiangsu, People's Republic of China
Received 2021 January 5; revised 2021 February 2; accepted 2021 February 4; published 2021 March 25

Abstract

We present the discovery and characterization of five hot and warm Jupiters—TOI-628 b (TIC 281408474; HD 288842), TOI-640 b (TIC 147977348), TOI-1333 b (TIC 395171208, BD+47 3521A), TOI-1478 b (TIC 409794137), and TOI-1601 b (TIC 139375960)—based on data from NASA's Transiting Exoplanet Survey Satellite (TESS). The five planets were identified from the full-frame images and were confirmed through a series of photometric and spectroscopic follow-up observations by the TESS Follow-up Observing Program Working Group. The planets are all Jovian size ($R_P = 1.01$–$1.77\ R_J$) and have masses that range from 0.85 to 6.33 M_J. The host stars of these systems have F and G spectral types ($5595 \leqslant T_{\rm eff} \leqslant 6460$ K) and are all relatively bright ($9.5 < V < 10.8$, $8.2 < K < 9.3$), making them well suited for future detailed characterization efforts. Three of the systems in our sample (TOI-640 b, TOI-1333 b, and TOI-1601 b) orbit subgiant host stars ($\log g < 4.1$). TOI-640 b is one of only three known hot Jupiters to have a highly inflated radius ($R_P > 1.7\ R_J$, possibly a result of its host star's evolution) and resides on an orbit with a period longer than 5 days. TOI-628 b is the most massive, hot Jupiter discovered to date by TESS with a measured mass of $6.31^{+0.28}_{-0.30}\ M_J$ and a statistically significant, nonzero orbital eccentricity of $e = 0.074^{+0.021}_{-0.022}$. This planet would not have had enough time to circularize through tidal forces from our analysis, suggesting that it might be remnant eccentricity from its migration. The longest-period planet in this sample, TOI-1478 b ($P = 10.18$ days), is a warm Jupiter in a circular orbit around a near-solar analog. NASA's TESS mission is continuing to increase the sample of well-characterized hot and warm Jupiters, complementing its primary mission goals.

Unified Astronomy Thesaurus concepts: Exoplanet astronomy (486); Exoplanet migration (2205); Exoplanet detection methods (489); Exoplanets (498); Transits (1711); Radial velocity (1332); Direct imaging (387)

Supporting material: data behind figure, machine-readable table

1. Introduction

The discovery of hot Jupiters, combined with the assumption that gas giant planets must form at separations from their host star similar to our own giant planets, indicated that giant planets likely undergo large-scale migration from their formation locations. Various mechanisms have been proposed to place giant planets into very short-period orbits (Goldreich & Tremaine 1980; Lin & Papaloizou 1986; Lin et al. 1996; see Dawson & Johnson 2018 for a detailed review). However, it is not clear which of these mechanisms (if any) are dominant or govern this migration, or whether hot Jupiters *can* form in situ (Batygin et al. 2016), obviating the need for large-scale migration. One possibility is that giant planets migrate slowly and smoothly within the circumstellar gas–dust disk, resulting in well-aligned, nearly circular orbits (D'Angelo et al. 2003). It is also thought that planetary migration may be heavily influenced by gravitational interactions with other bodies within the system. These interactions result in highly eccentric and misaligned orbits (relative to the rotation axis of the star) and are typically referred to as a type of "high-eccentricity migration" (HEM) or "Kozai–Lidov" (Lidov 1962; Kozai 1962; Rasio & Ford 1996; Wu & Murray 2003; Fabrycky & Tremaine 2007; Nagasawa & Ida 2011; Wu & Lithwick 2011; Naoz 2016). For short-period hot Jupiters, with periods less than about 5 days, the orbits will circularize in only a few billion years, erasing the evidence of HEM. Additionally, these

[68] Juan Carlos Torres Fellow.
[69] National Science Foundation Graduate Research Fellow.
[70] Eberly Research Fellow.

interactions can cause misalignments in the planet's orbital plane (relative to the original disk plane) that can remain present for much longer, and such misalignments can be detected through Doppler spectroscopy, using observations of the Rossiter–McLaughlin effect (McLaughlin 1924; Rossiter 1924) or Doppler tomography (e.g., Miller et al. 2010; Johnson et al. 2014; Zhou et al. 2016). Longer-period, hot ($P \gtrsim 5$ days) and warm ($P > 10$ days) Jupiters experience smaller tidal forces, preserving their orbital eccentricities. It is likely that multiple mechanisms shape the short-period giant planet population, and studying these longer-period hot Jupiters may give clues to their common evolutionary pathway.

While some ground-based transit surveys that were dedicated to discovering hot Jupiters had near 24 hr coverage (Bakos et al. 2013), in general they struggled to discover planets with periods $\gtrsim$5 days due to the poor duty cycle from weather and only being able to observe at night (Gaudi et al. 2005). Additionally, many of the first hot Jupiters discovered were assumed to reside in circular orbits when analyzing the observations, an assumption that may confuse current efforts to understand migration. Fortunately, NASA's Transiting Exoplanet Survey Satellite (TESS) mission was launched in 2018 April and completed its primary 2 yr long mission in 2020 July (Ricker et al. 2015). TESS was awarded a 27 month first extended mission in which it will not only reobserve some areas covered in the primary mission but also observe most of the ecliptic plane, nearly completing coverage of the entire sky. TESS has a minimum observing baseline of ~27 days, and from recent occurrence-rate studies, TESS planet searches will be mostly complete for hot Jupiters with periods $\lesssim$10 days (Zhou et al. 2019). Therefore, TESS provides a great resource for the discovery and confirmation of new longer-period hot and warm Jupiters ($5 < P < 15$ days), where eccentricities from migration would not be completely erased by tidal forces. TESS has already discovered a number of statistically significant hot Jupiters with highly eccentric ($e > 0.2$) orbits like HD 2685 b (Jones et al. 2019), TOI-172 b (Rodriguez et al. 2019), TOI-150 b (Kossakowski et al. 2019), TIC 237913194 b (Schlecker et al. 2020), and TOI-559 b (Ikwut-Ukwa et al. 2021). Additionally, TESS recently confirmed that the hot Jupiter HD 118203 b, an RV-identified planet with high eccentricity discovered with the radial velocity method (da Silva et al. 2006), transits its host star (Pepper et al. 2020).

TESS will also provide the ability to study hot-Jupiter reinflation since its high photometric precision will allow it to discover giant planets around larger, more evolved host stars. As a star evolves off the main sequence, the stellar irradiation received by warm Jupiters is similar to that of a hot Jupiter. Therefore, discovering gas giant planets orbiting evolved stars at longer periods (10 s of days) can test whether this increased irradiation causes the same inflation seen for short-period hot Jupiters (Lopez & Fortney 2016). Most warm Jupiters orbiting main-sequence stars show little to no inflation (Demory & Seager 2011), suggesting that this energy must be transferred deep into the planet's interior (Liu et al. 2008; Spiegel & Burrows 2013), and as the star evolves, these warm Jupiters may reinflate from the increased irradiation. Recent discoveries of hot Jupiters orbiting evolved stars are suggestive of reinflation (Almenara et al. 2015; Grunblatt et al. 2016; Hartman & Bakos 2016; Stevens et al. 2017), and TESS has already found a few hot and warm Jupiters orbiting evolved stars (Brahm et al. 2019; Huber et al. 2019; Nielsen et al. 2019; Rodriguez et al. 2019; Wang et al. 2019; Sha et al. 2021).

In this paper we present the discovery of TOI-628 b, TOI-640 b, TOI-1333 b, TOI-1478 b, and TOI-1601 b, five new hot and warm Jupiters from NASA's TESS mission. All five planets were discovered from an analysis of the 30 minute cadence full-frame images (FFIs) and first identified as TESS Objects of Interest (TOIs) by the TESS Science Office.[71] These five new systems increase the known sample of well-characterized hot Jupiters, particularly those with longer orbital periods (>5 days). In Section 2 we present our time-series photometric and spectroscopic observations obtained by the TESS Follow-up Observing Program (TFOP) Working Group (WG) and describe the high-spatial-resolution imaging of all five targets, specifically on TOI-1333 and its two nearby companions. Our methodology for our global modeling using `EXOFASTv2` (Eastman et al. 2019) is summarized in Section 3. We place these systems in context with the known population of hot and warm Jupiters and discuss the impact of TESS on the discovery of giant planets in Section 7, and our conclusions are given in Section 5.

2. Observations and Archival Data

We used a series of photometric and spectroscopic observations to confirm and characterize the new systems, including high-spatial-resolution imaging to rule out false positives, confirm them as bona fide planets, and measure key parameters such as orbital eccentricity and the planet's density. See Table 1 for a list of the literature kinematics and magnitudes for each target.

2.1. TESS Photometry

The initial detection of the new planets came from data collected by the TESS mission. TESS images the sky with a $24^\circ \times 96^\circ$ field of view and observes the same stars for about a month before moving on to observe a different region. During its primary mission, TESS saved and downloaded images of a smaller number of preselected stars every two minutes, while downloading coadded images of its entire field of view every 30 minutes. None of the planets described in this paper orbit stars that were preselected for two-minute cadence observations, so we use data from the 30 minute cadence FFIs.

After the data were transferred from the orbiting spacecraft back to Earth, the FFIs were calibrated using the TICA software (M. Fausnaugh et al. 2021, in preparation), and light curves for a set of stars complete down to TESS-band magnitude = 13.5 were extracted with the MIT Quick Look Pipeline (QLP; Huang et al. 2020b). The QLP extracts light curves from the FFIs using a difference image analysis technique. After removing the effects of scattered earthshine and moonshine from the images, the QLP subtracts a high-quality reference image from each individual science frame and measures difference fluxes within sets of photometric apertures surrounding each star in the image. These difference fluxes are then converted to absolute brightness measurements by adding back the median flux expected from each star based on its TESS-band magnitude. The QLP light curves have been used to discover dozens of planets (e.g., Huang et al. 2018; Rodriguez et al. 2019; Huang et al. 2020a) and a few thousand planet

[71] https://tess.mit.edu/toi-releases/toi-release-general/

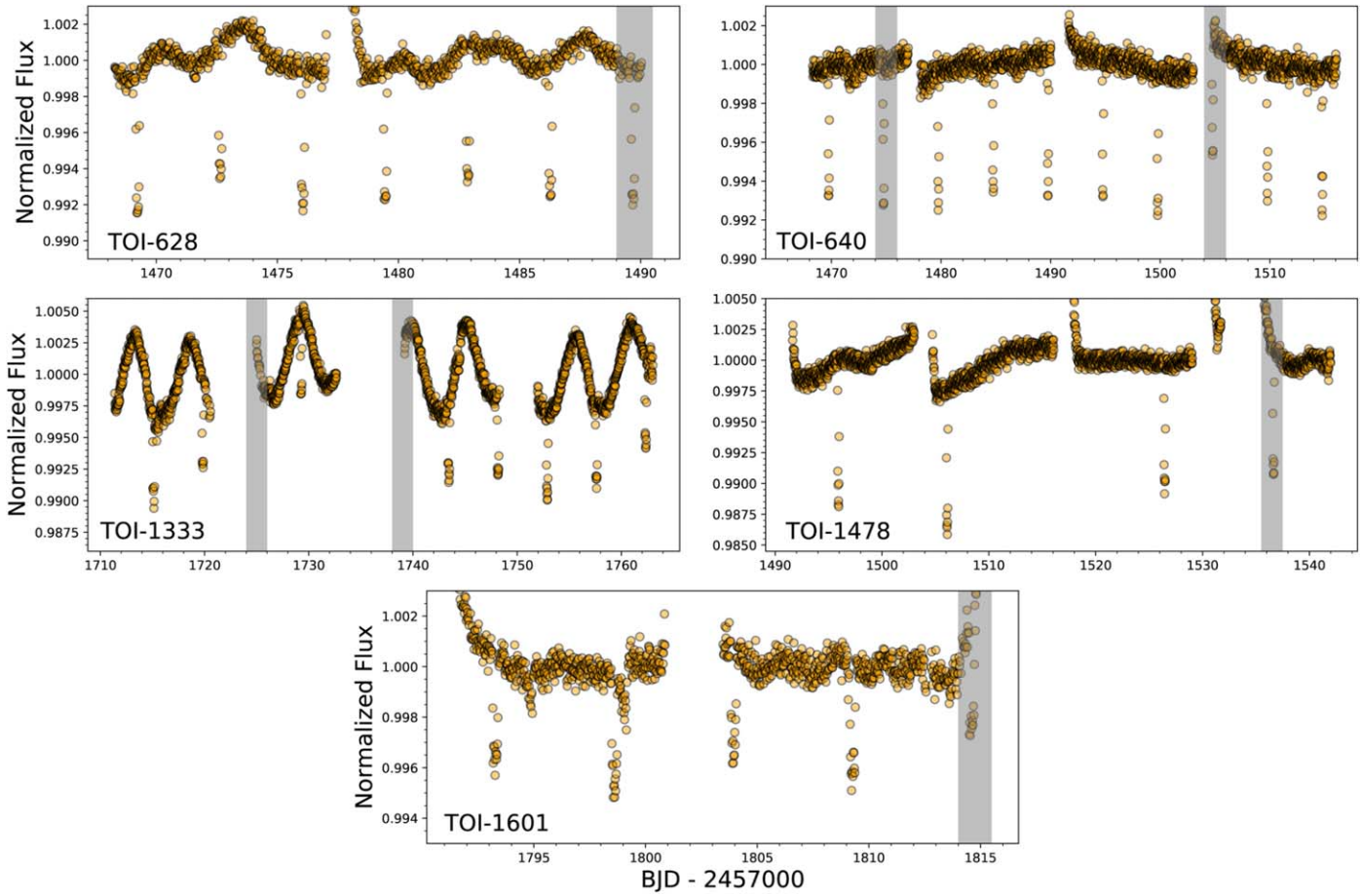

Figure 1. Raw TESS QLP 30 minute light curves for (top left) TOI-628, TOI-640 (top right), TOI-1333 (middle left), TOI-1478 (middle right), and TOI-1601 (bottom). Transits highlighted in gray were excluded from the global fit since they were flagged as bad quality by the QLP pipeline (Huang et al. 2020b).

candidates (Guerrero et al. 2021). Additional information and a description of the QLP procedures are given by Huang et al. (2020b). The QLP light curves are shown in Figure 1. All five of these light curves were flattened using *Keplerspline*,[72] a spline fitting routine to divide out the best-fit stellar variability (Vanderburg & Johnson 2014). The spacing of the spline break points for each system was determined by minimizing the Bayesian information criterion following the methodology from Shallue & Vanderburg (2018). After removing the stellar variability, we keep all data from one full transit duration before the transit until one full transit duration after the transit, and we discard the remaining baseline data (which contains very little useful information but is computationally expensive to model). We use these light-curve segments for the global fitting of each system (see Section 3).

Because the QLP uses aperture photometry on difference frames using a median-combined reference image, it does not always measure absolute transit depths, only difference fluxes. Transit depths measured by QLP, especially in crowded fields, might be dependent on the accuracy of the TESS-band magnitudes from the TESS Input Catalog (Stassun et al. 2018) to correct for contamination due to blending of nearby stars within the aperture. To check that the transit depths measured by QLP for these targets are reasonably accurate, we performed a spot check for TOI-1601 with light curves extracted using a more traditional simple aperture photometry method (Vanderburg et al. 2019). We did not deblend the photometry in this test because TOI-1601 is in a relatively sparse field, as shown from our high-resolution imaging (see Section 2.6.2). We ran an independent `EXOFASTv2` fit for TOI-1601 b (swapping this light curve for the QLP one) following the strategy discussed in Section 3, and the results were consistent to within $<1\sigma$ uncertainties. Additionally, for each system, we used the follow-up ground-based photometry within the global analysis to also constrain the depth, providing independent constraints that can be used to confirm the QLP depths (since the TFOP photometry is at a higher angular resolution than TESS). Within our global fit, we checked on any unknown contamination by fitting for a dilution term on the TESS bandpass to account for any difference compared to the SG1 photometry. In all cases other than TOI-1478, the fitted dilution was consistent with zero and well within our Gaussian 10% prior around zero, showing clear consistency between TESS and the TFOP seeing-limited photometry. TOI-1478 showed a significant Required dilution on the order of 12%. To properly account for this, we removed the TESS dilution prior (see Section 3 for details), allowing it to be a free parameter, to properly correct for this within the fit.

We searched the nonflattened QLP light curves for rotation-based modulations using the `VARTOOLS` Lomb–Scargle function (Hartman & Bakos 2016). Specifically, we searched from 0.1 to 30 days and detect a clear, strong periodicity at

[72] https://github.com/avanderburg/keplerspline

5.296 days for TOI-1333, significantly different from the orbital period of its planetary companion ($P_b = 4.72$ days). This same periodicity is observed in our ground-based photometry, ruling out any systematics in the TESS observations. We see some tentative evidence of a periodicity at 10–11 days for TOI-628, but it was only observed in one TESS sector.

2.2. WASP Photometry

The WASP transit search consisted of two wide-field arrays of eight cameras, with SuperWASP on La Palma covering the northern sky and WASP-South in South Africa covering the south (Pollacco et al. 2006). Each camera used a 200 mm, $f/1.8$ lens with a broadband filter spanning 400–700 nm, backed by 2048×2048 CCDs giving a plate scale of $13\farcs7$ pixel^{-1}. Observations then rastered available fields with a typical 15 minute cadence.

We searched the WASP data for any rotational modulations using the methods from Maxted et al. (2011). TOI-640 was observed for spans of 150 nights in each of four years. The data from 2008, 2009, and 2010 show no significant modulation. The data from 2007, however, show significant power at a period of 62 ± 5 days, with an amplitude of 3 mmag and an estimated false-alarm probability below 1%. Since this is seen in only one season, and given that the data span only 2.5 cycles, we do not regard this detection as fully reliable. For TOI-1333, the WASP data span 130 days in 2007 and show a clear modulation with a period of 15.9 ± 0.3 days, an amplitude of 19 mmag, and a false-alarm probability below 1%. A similar periodicity is also seen in the TESS data and in the Kilodegree Extremely Little Telescope (KELT) data (see below) but at one-third of this period at 5.3 days. No significant periodicity was detected for TOI-1478 or TOI-1601.

Given knowledge of the TESS detections, transits of three of the systems described here can be found readily in the WASP data. TOI-640 was observed between 2006 and 2012, accumulating 23,000 data points. The WASP search algorithm (Collier Cameron et al. 2007) finds the transit with a period of 5.003773 ± 0.000041 and a midtransit epoch (T_C) of $2454822.00318 \pm 0.00411$ $\mathrm{HJD_{TDB}}$. This detection had been overlooked by WASP vetters owing to the near-integer day period (5.00 days), since the dominant red noise in the WASP data is at multiples of a day. TOI-1478 was observed between 2009 and 2012, accumulating 9000 data points, less than usual for WASP since the field is near the crowded Galactic plane. It had not been flagged as a WASP candidate, but the search algorithm finds the transit with a period of 10.18051 ± 0.00017 days and a T_C of $2455696.36710 \pm 0.00492$ $\mathrm{HJD_{TDB}}$. TOI-1601 was observed over 2006 and 2007, accumulating 10,400 data points. The search algorithm finds the transit and gets a period of 5.33197 ± 0.00010 and a T_C of $2454186.65253 \pm 0.01283$ $\mathrm{HJD_{TDB}}$. We use these T_C values as priors for the `EXOFASTv2` global fits of TOI-640 b, TOI-1478 b, and TOI-1601 b. We see an ~40% reduction in uncertainty on the period of the planet when including the WASP T_C prior.

2.3. KELT Photometry

To complement the TESS photometry, we analyzed observations of these five TOIs from the KELT survey[73] (Pepper et al. 2007, 2012, 2018). For a full description of the KELT observing strategy and reduction process, see Siverd et al. (2012) and Kuhn et al. (2016). KELT has two fully robotic telescopes, each of which uses a Mamiya 645 80 mm $f/1.9$ lens with 42 mm aperture and Apogee 4 k × 4 k CCD on a Paramount ME mount. This setup provides a $26° \times 26°$ field of view with a $23''$ pixel scale. The two telescopes are located at Winer Observatory in Sonoita, AZ and at the South African Astronomical Observatory (SAAO) in Sutherland, South Africa. KELT covers ~85% of the entire sky, and the observing strategy results in a 20–30 minute cadence. Some of the KELT light curves are publicly available through the NASA Exoplanet Archive. KELT observations were available for TOI-628, TOI-1333, TOI-1478, and TOI-1601. KELT-South observed TOI-628 2828 times and TOI-1478 4632 times from 2010 to 2015. KELT-North observed TOI-1333 from 2012 to 2014 and TOI-1601 from 2006 to 2014, acquiring 2580 and 8520 observations, respectively. Since KELT has been observing since 2006 in some cases, the observations significantly extend the baseline of the photometry and can provide a strong constraint on the ephemeris of each system. Following the strategy described in Siverd et al. (2012) and Kuhn et al. (2016), we also search the KELT light curves for transits of each planet. Unfortunately, no significant signs of the known planetary transits were found, likely due to the poor duty cycle for longer orbital periods.

Following the approach of Stassun et al. (1999) and Oelkers et al. (2018), we executed a search for periodic signals most likely to come from the rotation period of the star. For these stars, we postprocessed the light-curve data using the Trend-Filtering Algorithm (Kovács et al. 2005) to remove common systematics. We then searched for candidate rotation signals using a modified version of the Lomb–Scargle period-finder algorithm (Lomb 1976; Scargle 1982). We searched for periods between a minimum period of 0.5 days and a maximum period of 50 days using 2000 frequency steps.[74] We masked periods between 0.5 and 0.505 days and 0.97–1.04 days to avoid the most common detector aliases associated with KELT's observational cadence and its interaction with the periods for the solar and sidereal day. For each star, we selected the highest statistically significant peak of the power spectrum (hereafter γ) as the candidate period.

We then executed a bootstrap analysis, using 1000 Monte Carlo iterations, where the dates of the observations were not changed but the magnitude values of the light curve were randomized, following the work of Henderson & Stassun (2012). We recalculated the Lomb–Scargle power spectrum for each iteration and recorded the maximum peak power (hereafter $\gamma_{\rm sim}$) of all iterations. If the highest power spectrum peak was larger than the maximum simulated peak ($\gamma > \gamma_{\rm sim}$) after 1000 iterations, we considered the periodic signal to be a candidate rotation period.

We find TOI-1333 to have a strongly significant ($\gamma > 50$) candidate rotation period at 5.3 days, which is consistent with TESS (see Section 2.1), and TOI-1601 and TOI-1478 to have weakly significant ($\gamma > 10$) candidate rotation periods of 9.3 and 16.6 days, respectively. However, we do not see these periodicities in the TESS photometry, and they are likely aliases of the KELT observing strategy. KELT did not obtain observations of TOI-640.

[73] https://keltsurvey.org

[74] The total number of frequency steps may vary slightly depending on the number of data points in any given light curve.

2.4. Ground-based Photometry from the TESS Follow-up Observing Program Working Group

To refine the ephemerides and transit parameters for each system while ruling out false-positive scenarios, we obtained photometric follow-up observations on all five systems from the TESS Follow-up Observing Program Working Group[75] subgroup 1 (SG1) for seeing-limited photometry. Specifically, the follow-up comes from the Las Cumbres Observatory (LCO) telescope network (Brown et al. 2013), Whitin Observatory at Wellesley College, KeplerCam on the 1.2 m telescope at Fred Lawrence Whipple Observatory (FLWO), Brierfield Observatory, PEST Observatory, C. R. Chambliss Astronomical Observatory (CRCAO) at Kutztown University, Adams Observatory at Austin College, and Suto Observatory. To schedule the photometric transit follow-up observations, we used the `TAPIR` software package (Jensen 2013). The data reduction and aperture photometry extraction was performed using `AstroImageJ` (Collins et al. 2017) for all follow-up data other than the PEST observations, which were done using a custom software package `PEST Pipeline`.[76] The TFOP follow-up photometry for these five systems is shown in Figure 2, and a list of each telescope's information and details on each follow-up transit can be seen in Table 2. The follow-up transits presented in Figure 2 are available as machine-readable tables with this paper.

2.5. Spectroscopy

To rule out false-positive scenarios and measure the mass and orbital eccentricity of each system, we obtained time-series spectroscopy coordinated through the TFOP WGs. A sample of one radial velocity (RV) point per target per instrument is shown in Table 3, with the full table available in machine-readable form in the online journal. The RVs and best-fit models from our `EXOFASTv2` analysis are shown in Figure 3 (see Section 3). Following the methodology in Zhou et al. (2018), we measure the $v \sin I_*$ and macroturbulent broadening for all five systems from the Tillinghast Reflector Echelle Spectrograph except TOI-640, where the CHIRON observations were used (see Table 1).

2.5.1. TCES Spectroscopy

Reconnaissance spectroscopic observations of TOI-628 were carried out with the Tautenburg Coudé Echelle Spectrograph (TCES) mounted at the 2 m "Alfred Jensch" Telescope of the Thuringian State Observatory (TLS) in Tautenburg, Germany. The spectra cover the 470–740 nm wavelength range and have a resolution $R = 57{,}000$. A 40 minute exposure was taken at BJD = 2458777.6053 (orbital phase $\phi \sim 0.5$), and a 3×20 minute exposure at BJD = 2458855.3720 ($\phi \sim 0.0$). We measured for the two single-lined spectra at $\Delta\mathrm{RV} \lesssim 1$ km s^{-1}, ruling out an eclipsing binary as the cause of the event detected by TESS. These velocities were not included in the global fit for TOI-628.

2.5.2. TRES Spectroscopy

To confirm targets from TESS in the Northern hemisphere, we observed TOI-628, TOI-1333, TOI-1478, and TOI-1601 with the Tillinghast Reflector Echelle Spectrograph (TRES; Fűrész 2008)[77] on the 1.5 m Tillinghast Reflector. The telescope is located at the Fred L. Whipple Observatory on Mt. Hopkins, AZ, and the spectrograph has a resolving power of $R = 44{,}000$. See Buchhave et al. (2010) and Quinn et al. (2012) for a detailed description of the reduction and RV extraction pipeline. The only difference in our analysis is that we created the template spectra for the RV extraction by aligning and median-combining all of the out-of-transit spectra. We removed cosmic rays and cross-correlated the median-combined spectra against all of the observed spectra. Bisector spans for the TRES spectra were calculated following the technique described in Torres et al. (2007). There was no correlation between the bisector spans and the RVs. We also used the TRES spectra to provide constraints on the $T_{\rm eff}$ and [Fe/H] for our global analysis. We analyzed the TRES spectra with the Stellar Parameter Classification (SPC) package (Buchhave et al. 2012) to determine the metallicity and rotational velocity for all five host stars (see Tables 1 and 4). We also used SPC to determine a constraint on the $T_{\rm eff}$ of 6250 ± 100 K for TOI-1333, which is used in Section 2.6.4 to constrain the dilution from nearby companions and the radius of TOI-1333.

2.5.3. CHIRON Spectroscopy

We obtained a series of spectroscopic observations with the 1.5 m SMARTS/CHIRON facility (see Table 3; Tokovinin et al. 2013) for TOI-640 and TOI-1478 to measure the host star parameters and constrain their masses and eccentricities. The 1.5 m SMARTS facility is located at Cerro Tololo Inter-American Observatory (CTIO), Chile. CHIRON is a high-resolution echelle spectrograph fed via an image slicer through a single multimode fiber, with a spectral resolving power of $R \sim 80{,}000$ over the wavelength region from 410 to 870 nm. For the case of TOI-1478, we treat the pre- and postshutdown RVs as separate instruments within the fit (see Section 3).

To obtain the stellar atmospheric parameters, we matched the CHIRON spectra against an interpolated library of ~10,000 observed spectra classified by SPC (Buchhave et al. 2012). The metallicity from this analysis was used as a prior for the global fit of TOI-640 (see Table 4). RVs were derived via the least-squares deconvolution (Donati et al. 1997; Zhou et al. 2020) of the spectra against nonrotating synthetic templates matching the spectral parameters of each host star, generated using the ATLAS9 model atmospheres (Kurucz 1992). The RVs were then measured by fitting a least-squares deconvolution line profile with a rotational broadening kernel as prescribed by Gray (2005). The velocities for each system are presented in Table 3.

2.5.4. FEROS Spectroscopy

Using the FEROS spectrograph (Kaufer et al. 1999) mounted on the 2.2 m MPG telescope at La Silla observatory in Chile, we obtained eight observations of TOI-1478. FEROS has $R = 48{,}000$, and the observations were between UT 2020 March 2 and UT 2020 March 22. A ThAr+Ne lamp was used to illuminate the fiber simultaneously with the observations to determine the instrumental offset. We reduced the spectra,

[75] https://tess.mit.edu/followup/
[76] http://pestobservatory.com/the-pest-pipeline/
[77] http://www.sao.arizona.edu/html/FLWO/60/TRES/GABORthesis.pdf

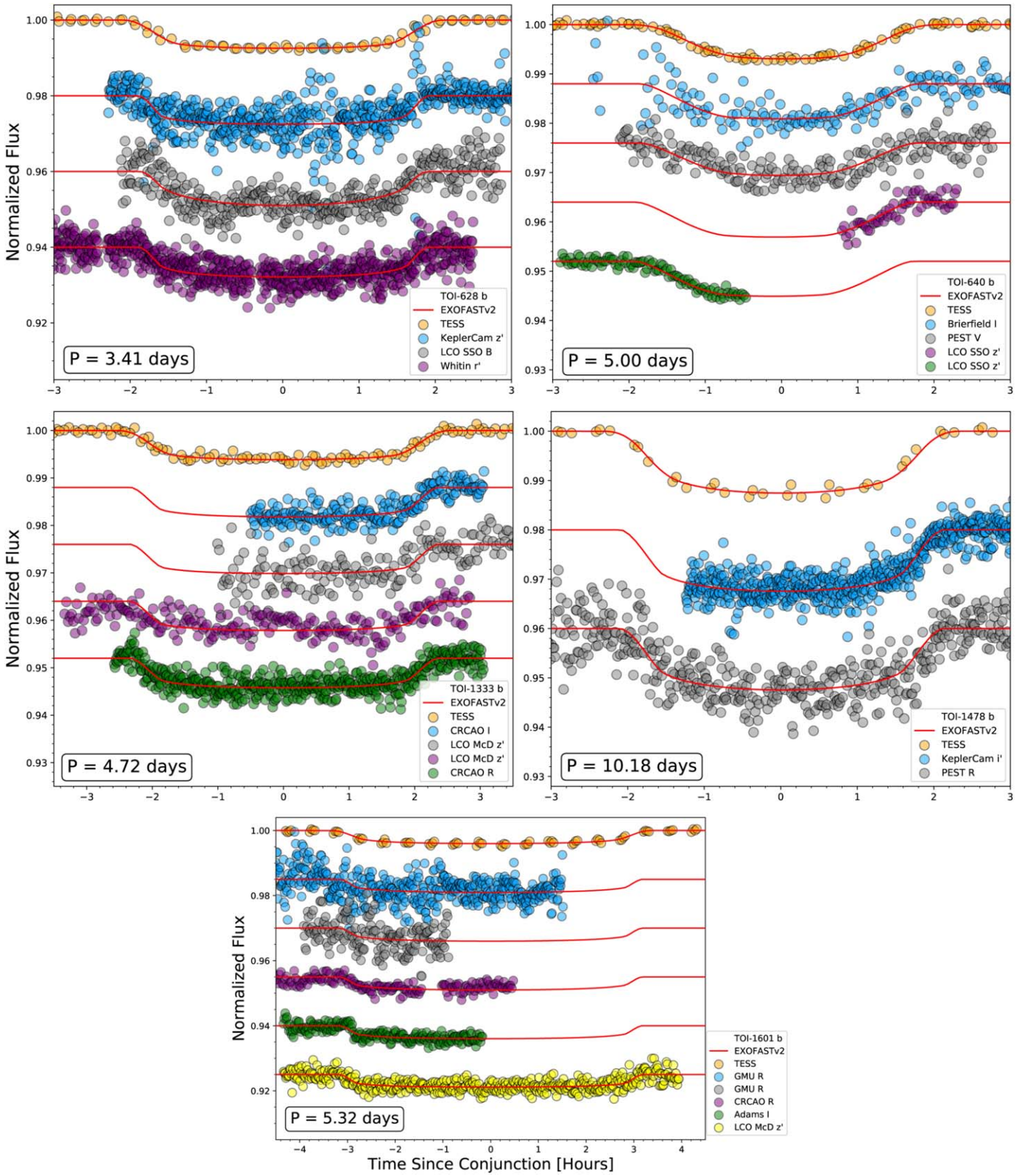

Figure 2. TESS (orange) and TFOP SG1 follow-up transits of TOI-628 b (top left), TOI-640 b (top right), TOI-1333 b (middle left), TOI-1478 b (middle right), and TOI-1601 b (bottom). The `EXOFASTv2` model for each transit observation is shown by the red solid line. The TFOP photometry is available as the Data behind the Figure.

(The data used to create this figure are available.)

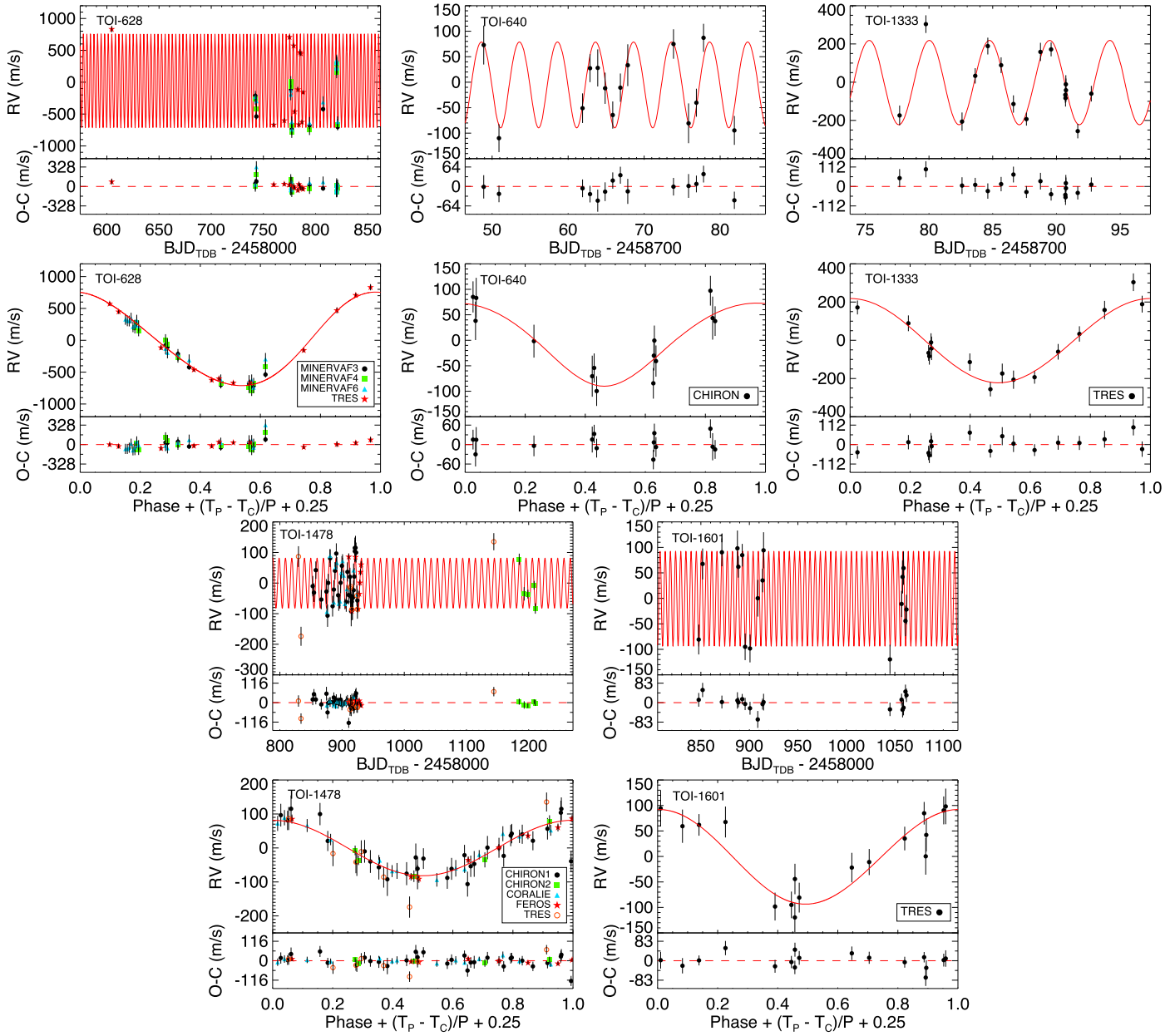

Figure 3. RV observations of TOI-628 (top left), TOI-640 (top middle), TOI-1333 (top right), TOI-1478 (bottom left), and TOI-1601 (bottom right). In each case, the top figure shows the RVs vs. time, and the bottom panel is phased to the best-fit ephemeris from our global fit. The EXOFASTv2 model is shown in red, and the residuals to the best fit are shown below each plot. We see no periodicity in the residuals from our fit.

derived the RVs, and produced the bisector spans using the CERES suite for echelle pipelines (Brahm et al. 2017).

2.5.5. CORALIE Spectroscopy

TOI-1478 was observed with the CORALIE high-resolution spectrograph ($R = 60{,}000$) on the Swiss 1.2 m Euler telescope at La Silla Observatories, Chile (Queloz et al. 2001). A total of 14 spectra were obtained between UT 2020 January 26 and March 16, covering several orbits of TOI-1478 b. CORALIE is fed by a 2″ science fiber and a secondary fiber with simultaneous Fabry–Perot for wavelength calibration. RVs were computed with the standard CORALIE data-reduction pipeline via cross-correlation with a binary G2 mask. Activity indices, bisector spans (BIS), and other line profile diagnostics were extracted as well. We find no correlation between the RVs and BIS, nor activity indicators. Our exposure times varied between 1200 and 1800 s depending on the site conditions and observing schedule.

2.5.6. MINERVA-Australis Spectroscopy

MINERVA-Australis is an array of four PlaneWave CDK700 telescopes located in Queensland, Australia, fully dedicated to the precise RV follow-up of TESS candidates. The four telescopes can be simultaneously fiber-fed to a single KiwiSpec R4-100 high-resolution ($R = 80{,}000$) spectrograph (Barnes et al. 2012; Addison et al. 2019, 2021). TOI-628 was monitored by MINERVA-Australis using two or three telescopes in the array (Minerva3, Minerva4, Minerva6) between UT 2019 September 15 and December 3. Each epoch consists of two 30 minute exposures, and the resulting RVs are binned to a single point, as shown by the example in Table 3. Telescopes 1 and 3 obtained seven RV epochs, while Telescope 4

Table 1
Literature and Measured Properties

Other Identifiers							
		TOI-628	TOI-640	TOI-1333	TOI-1478	TOI-1601	
		TIC 281408474	TIC 147977348	TIC 395171208	TIC 409794137	TIC 139375960	
		HD 288842	⋯	BD+47 3521A	⋯	⋯	
	TYCHO-2	TYC 0146-01523-1	TYC 7099-00846-1	TYC 3595-01186-1	TYC 5440-01407-1	TYC 2836-00689-1	
	2MASS	J06370314+0146031	J06385630-3638462	J21400351+4824243	J08254410-1333356	J02332674+4100483	
	TESS Sector	6	6,7	15,16	7,8	18	
Parameter	Description	Value	Value	Value	Value	Value	Source
α_{J2000}[a]	R.A. (R.A.)	06:37:03.13607	06:38:56.30742	21:40:03.50398	08:25:44.10708	02:33:26.74683	1
δ_{J2000}[a]	Decl. (decl.)	01:46:03.19552	−36:38:46.14425	48:24:24.52541	−13:33:35.42756	+41:00:48.36893	1
B_T	Tycho B_T mag.	10.782 ± 0.051	11.178 ± 0.05	9.933 ± 0.024	11.618 ± 0.082	11.521 ± 0.067	2
V_T	Tycho V_T mag.	10.176 ± 0.041	10.574 ± 0.043	9.487 ± 0.021	10.805 ± 0.067	10.710 ± 0.051	2
G	Gaia G mag.	10.0579 ± 0.02	10.4006 ± 0.02	9.35 ± 0.02	10.66 ± 0.02	10.53 ± 0.02	1
B_P	Gaia B_P mag.	10.38 ± 0.02	10.68 ± 0.02	9.59 ± 0.02	11.03 ± 0.02	10.86 ± 0.02	1
R_P	Gaia R_P mag.	9.61 ± 0.02	9.99 ± 0.02	8.99 ± 0.02	10.16 ± 0.02	10.06 ± 0.02	1
T	TESS mag.	9.6565 ± 0.0066	10.0367 ± 0.006	9.03527 ± 0.0061	10.2042 ± 0.006	10.1035 ± 0.0065	3
J	2MASS J mag.	9.170 ± 0.041	9.519 ± 0.024	8.485 ± 0.027	9.590 ± 0.023	9.505 ± 0.022	4
H	2MASS H mag.	8.895 ± 0.057	9.327 ± 0.026	8.397 ± 0.043	9.255 ± 0.026	9.266 ± 0.021	4
K_S	2MASS K_S mag.	8.811 ± 0.02	9.243 ± 0.023	8.272 ± 0.024	9.201 ± 0.021	9.19 ± 0.02	4
WISE1	WISE1 mag.	8.76 ± 0.03	9.213 ± 0.03	7.706 ± 0.013	9.15 ± 0.03	9.16 ± 0.03	5
WISE2	WISE2 mag.	8.79 ± 0.03	9.240 ± 0.03	7.594 ± 0.012	9.19 ± 0.03	9.21 ± 0.03	5
WISE3	WISE3 mag.	8.59 ± 0.03	9.239 ± 0.03	8.035 ± 0.019	9.18 ± 0.03	9.18 ± 0.034	5
WISE4	WISE4 mag.	8.23 ± 0.19	⋯	8.043 ± 0.163	⋯	8.80 ± 0.33	5
μ_α	Gaia DR2 proper motion in R.A. (mas yr^{-1})	-1.437 ± 0.117	-3.872 ± 0.040	-9.810 ± 0.050	-8.277 ± 0.058	21.708 ± 0.095	1
μ_δ	Gaia DR2 proper motion in decl. (mas yr^{-1})	-1.082 ± 0.087	4.927 ± 0.045	-10.501 ± 0.046	67.943 ± 0.046	-0.874 ± 0.090	1
$v \sin i_\star$	Rotational velocity (km s^{-1})	6.9 ± 0.5	6.1 ± 0.5	14.2 ± 0.5	4.3 ± 0.5	6.4 ± 0.5	Sections 2.5.2, 2.5.2 and 2.5.3
v_{mac}	Macroturbulent broadening (km s^{-1})	5.4 ± 0.7	6.32 ± 1.37	7.4 ± 1.8	4.9 ± 0.5	6.3 ± 0.6	Sections 2.5.2, 2.5.2 and 2.5.3
π[b]	Gaia parallax (mas)	5.601 ± 0.103	2.925 ± 0.033	4.989 ± 0.038	6.542 ± 0.047	2.974 ± 0.080	1
P_{Rot}	Rotation period (days)			5.3 ± 0.159			Sections 2.1, 2.2, and 2.3

Notes. The uncertainties of the photometry have a systematic error floor applied.
[a] R.A. and decl. are in epoch J2000. The coordinates come from Vizier, where the Gaia R.A. and decl. have been precessed and corrected to J2000 from epoch J2015.5.
[b] Values have been corrected for the −0.30 μas offset as reported by Lindegren et al. (2018).
References are (1) Gaia Collaboration et al. (2018), (2) Høg et al. (2000), (3) Stassun et al. (2018), (4) Cutri et al. (2003), (5) Zacharias et al. (2017).

Table 2
Photometric Follow-up Observations of These Systems Used in the Global Fits and the Detrending Parameters

Target	Observatory	Date (UT)	Size (m)	Filter	FOV	Pixel Scale	Exp (s)	Additive Detrending
TOI-628 b	FLWO/KeplerCam	2019 Dec 6	1.2	z'	$23\farcm1 \times 23\farcm1$	$0\farcs672$	9	None
TOI-628 b	LCO TFN	2019 Dec 16	0.4	z'	$19' \times 29'$	$0\farcs57$	18	air mass
TOI-628 b	Whitin	2020 Feb 8	0.7	r'	$24' \times 24'$	$0\farcs67$	10	air mass
TOI-640 b	Brierfield	2019 Dec 27	0.36	I	$49\farcm4 \times 49\farcm4$	$1\farcs47$	90	X(FITS), Y(FITS)
TOI-640 b	PEST	2020 Mar 1	0.3048	R	$31' \times 21'$	$1\farcs2$	60	none
TOI-640 b	LCO SSO	2020 Aug 23	1.0	z'	$27' \times 27'$	$0\farcs39$	60	Y(FITS)
TOI-640 b	LCO SSO	2020 Nov 6	1.0	z'	$27' \times 27'$	$0\farcs39$	60	air mass
TOI-1333 b	CRCAO	2020 Jul 29	0.6096	I	$26\farcm8 \times 26\farcm8$	$0\farcs39$	45	air mass
TOI-1333 b	LCO McDonald	2020 Jul 29	0.4	z'	$19' \times 29'$	$0\farcs57$	30	total counts
TOI-1333 b	LCO McDonald	2020 Aug 12	0.4	z'	$19' \times 29'$	$0\farcs57$	30	Y(FITS)
TOI-1333 b	CRCAO	2020 Sep 19	0.6096	z'	$26\farcm8 \times 26\farcm8$	$0\farcs39$	80	air mass
TOI-1478 b	FLWO/KeplerCam	2019 Dec 14	1.2	i'	$23\farcm1 \times 23\farcm1$	$0\farcs672$	7	none
TOI-1478 b	PEST	2020 Jan 3	0.3048	R	$31' \times 21'$	$1\farcs2$	30	air mass
TOI-1601 b	GMU	2020 Aug 30	0.8	R	$23' \times 23'$	$0\farcs34$	30	air mass, sky/pixels
TOI-1601 b	GMU	2020 Sep 15	0.8	R	$23' \times 23'$	$0\farcs34$	30	air mass, sky/pixels, X(FITS)
TOI-1601 b	CRCAO	2020 Oct 1	0.6096	z'	$26\farcm8 \times 26\farcm8$	$0\farcs39$	90	air mass
TOI-1601 b	Adams	2020 Oct 17	0.61	I	$26' \times 26'$	$0\farcs38$	60	air mass, total counts
TOI-1601 b	LCO McDonald	2020 Oct 17	1.0	z'	$27' \times 27'$	$0\farcs39$	60	air mass, sky/pixels

Note. All of the follow-up photometry presented in this paper is available as the Data behind Figure 2 in machine-readable form in the online journal. See Section D in the Appendix of Collins et al. (2017) for a description of each detrending parameter.

Table 3
First RV Point from Each Spectrograph for All Five Systems

BJD_{TDB}	RV (m s^{-1})	σ_{RV}[a] (m s^{-1})	Target	Instrument
2458604.64716	193.0	43.6	TOI-628	TRES
2458742.25270	19775.2	17.5	TOI-628	MINERVA3
2458742.25270	19700.8	14.3	TOI-628	MINERVA4
2458742.25270	19795.7	41.0	TOI-628	MINERVA6
2458748.89482	39168.0	29.4	TOI-640	CHIRON
2458777.69583	−50.6	48.0	TOI-1333	TRES
2458852.80172	19374.4	21.9	TOI-1478	CHIRON
2458875.60994	20738.5	22.0	TOI-1478	CORALIE
2458910.73537	20910.3	7.5	TOI-1478	FEROS
2458829.86525	67.4	27.6	TOI-1478	TRES
2459184.83629	19502.0	24.0	TOI-1478	CHIRON2
2458847.77575	−184.1	32.0	TOI-1601	TRES

Note.
[a] The internal RV error for the observation shown.

(This table is available in its entirety in machine-readable form.)

obtained four epochs. RVs for the observations are derived for each telescope by cross-correlation, where the template being matched is the mean spectrum of each telescope. The instrumental variations are corrected by using the RVs computed from different Minerva telescopes as originating from independent instruments within our global model.

2.6. High-resolution Imaging

As part of our standard process for validating transiting exoplanets to assess possible contamination of bound or unbound companions on the derived planetary radii (Ciardi et al. 2015), we obtained high-spatial-resolution imaging observations of all five systems.

2.6.1. Speckle Imaging

We searched for close companions to TOI-628, TOI-640, and TOI-1478 with speckle imaging in the I band on the 4.1 m Southern Astrophysical Research (SOAR) telescope (Tokovinin 2018). The speckle imaging was conducted using HRCam (field of view of 15″) and had a $0\farcs01575$ pixel scale. TOI-628 was observed on UT 2019 November 11 with a sensitivity of $\Delta\mathrm{Mag} = 7.2$ at 1″. Speckle observations of TOI-640 were taken on UT 2019 May 18 and had an estimated contrast of $\Delta\mathrm{mag} = 6.6$ at 1″. Observations of TOI-1478 were taken on UT 2020 January 7 and had an estimated contrast of $\Delta\mathrm{mag} = 6.8$ at 1″. See Ziegler et al. (2020) for a description of the general observing strategy for TESS targets. No nearby companion was observed for any of the three targets out to 3″.

We also obtained two sets of high-resolution speckle images of TOI-1478. One was collected on UT 2020 January 14 using the Zorro instrument mounted on the 8 m Gemini South telescope located on the summit of Cerro Pachon in Chile and the other on UT 2020 February 18 using the Alopeke instrument mounted on the 8 m Gemini-North telescope located on the summit of Maunakea in Hawaii. These twin instruments simultaneously observe in two bands, $\frac{\lambda}{\Delta\lambda} = 832/40$ nm and 562/54 nm, obtaining diffraction limited images with inner working angles $0\farcs026$ and $0\farcs017$, respectively. Each observation consisted of 6 minutes of total integration time at each telescope taken as sets of 1000×0.06 second images. All of the images were combined and subjected to Fourier analysis, leading to the production of final data products including speckle reconstructed imagery (see Howell et al. 2011). Both speckle imaging results showed similar contrast limits and revealed that TOI-1478 is a single star to contrast limits of 5–9 mag (out to $1\farcs17$), ruling out most main-sequence companions to TOI-1478 within the spatial limits of ∼4–180 au (for $d = 153$ pc, as determined from the Gaia DR2 parallax; Gaia Collaboration et al. 2018).

2.6.2. Adaptive Optics Imaging

We observed TOI-628 on UT 2019 November 11 using the ShARCS adaptive optics system on the 3 m Shane Telescope at Lick Observatory. ShARCS has a field of view of $20'' \times 20''$

Table 4
Median Values and 68% Confidence Intervals for the Global Models

Priors:		TOI-628 b	TOI-640 b	TOI-1333 b[a]	TOI-1478 b[b]	TOI-1601 b	
Gaussian	[c] Gaia parallax (mas)	5.601 ± 0.103	2.925 ± 0.033	⋯	6.542 ± 0.047	2.974 ± 0.080	
Gaussian	[Fe/H] Metallicity (dex)	0.24 ± 0.08	0.02 ± 0.1	0.11 ± 0.08	0.07 ± 0.08	0.31 ± 0.08	
Upper Limit	A_V V-band extinction (mag)	2.977	0.292	⋯	0.120	0.14694	
Gaussian	$R_\star$ Stellar radius ($R_\odot$)	⋯	⋯	1.963 ± 0.064	⋯	⋯	⋯
Gaussian	$T_{\rm eff}$ Stellar effective temperature (K)	⋯	⋯	6250 ± 100	⋯	⋯	⋯
Gaussian	T_C[d] Time of conjunction ($\rm HJD_{TDB}$)	⋯	$2454822.00318 \pm 0.00411$	⋯	$2455696.36710 \pm 0.00492$	$2454186.65253 \pm 0.01283$	
Gaussian[e]	D_T Dilution in TESS	0.00000 ± 0.00344	0.00000 ± 0.00360	0.00000 ± 0.03817	⋯	0.0 ± 0.00196	
Gaussian[f]	D_I Dilution in I	⋯	⋯	0.3609 ± 0.0180	⋯	⋯	
Gaussian[f]	D_R Dilution in R	⋯	⋯	0.3499 ± 0.0175	⋯	⋯	
Gaussian[f]	$D_{z'}$ Dilution in z'	⋯	⋯	0.0664 ± 0.0033	⋯	⋯	
Parameter	Units	Values					
Stellar Parameters:							
Probability		100%	100%	100%	100%	68.4%	31.6%
M_*	Mass ($M_\odot$)	$1.311^{+0.066}_{-0.075}$	$1.536^{+0.069}_{-0.076}$	$1.464^{+0.076}_{-0.079}$	$0.947^{+0.059}_{-0.041}$	$1.517^{+0.053}_{-0.049}$	$1.340^{+0.042}_{-0.045}$
R_*	Radius ($R_\odot$)	$1.345^{+0.046}_{-0.040}$	$2.082^{+0.064}_{-0.058}$	$1.925^{+0.064}_{-0.063}$	$1.048^{+0.030}_{-0.029}$	$2.186^{+0.074}_{-0.063}$	$2.185^{+0.086}_{-0.080}$
L_*	Luminosity ($L_\odot$)	$2.48^{+0.41}_{-0.28}$	$6.83^{+0.41}_{-0.54}$	$5.17^{+0.49}_{-0.45}$	$0.971^{+0.036}_{-0.035}$	$5.40^{+0.35}_{-0.33}$	$5.25^{+0.35}_{-0.33}$
$F_{\rm Bol}$	Bolometric flux $\times 10^{-9}$ (cgs)	$2.52^{+0.39}_{-0.27}$	$1.87^{+0.10}_{-0.14}$	⋯	1.32 ± 0.45	$1.505^{+0.52}_{-0.61}$	$1.485^{+0.59}_{-0.61}$
ρ_*	Density (cgs)	$0.762^{+0.067}_{-0.078}$	$0.240^{+0.024}_{-0.025}$	$0.289^{+0.031}_{-0.028}$	$1.16^{+0.14}_{-0.11}$	$0.205^{+0.016}_{-0.018}$	$0.181^{+0.020}_{-0.019}$
$\log g$	Surface gravity (cgs)	$4.300^{+0.026}_{-0.036}$	$3.987^{+0.030}_{-0.036}$	$4.034^{+0.032}_{-0.033}$	$4.374^{+0.039}_{-0.032}$	$3.940^{+0.022}_{-0.025}$	$3.885^{+0.029}_{-0.031}$
$T_{\rm eff}$	Effective temperature (K)	6250^{+220}_{-190}	6460^{+130}_{-150}	6274 ± 97	5597^{+83}_{-82}	5948^{+87}_{-89}	5910^{+96}_{-99}
[Fe/H]	Metallicity (dex)	$0.258^{+0.078}_{-0.080}$	$0.072^{+0.085}_{-0.076}$	$0.119^{+0.078}_{-0.077}$	$0.078^{+0.072}_{-0.066}$	$0.329^{+0.073}_{-0.075}$	0.299 ± 0.076
$[\rm Fe/H]_0$[g]	Initial metallicity	$0.271^{+0.070}_{-0.068}$	$0.174^{+0.088}_{-0.080}$	$0.212^{+0.083}_{-0.084}$	$0.110^{+0.069}_{-0.064}$	0.347 ± 0.069	$0.296^{+0.070}_{-0.069}$
Age	Age (Gyr)	$1.28^{+1.6}_{-0.91}$	$1.99^{+0.55}_{-0.40}$	$2.33^{+0.71}_{-0.56}$	$9.1^{+3.1}_{-3.9}$	$2.64^{+0.38}_{-0.39}$	$4.27^{+0.53}_{-0.42}$
EEP[h]	Equal evolutionary phase	331^{+31}_{-37}	380^{+19}_{-17}	381^{+20}_{-21}	400^{+16}_{-37}	$403.1^{+7.9}_{-11}$	$452.9^{+4.3}_{-5.2}$
A_V	V-band extinction (mag)	$0.22^{+0.18}_{-0.14}$	$0.217^{+0.055}_{-0.095}$	⋯	$0.062^{+0.039}_{-0.041}$	$0.103^{+0.032}_{-0.053}$	$0.086^{+0.043}_{-0.053}$
$\sigma_{\rm SED}$	SED photometry error scaling	$3.27^{+1.2}_{-0.73}$	$0.84^{+0.35}_{-0.22}$	⋯	$0.70^{+0.29}_{-0.17}$	$1.17^{+0.42}_{-0.27}$	$1.20^{+0.44}_{-0.27}$
ϖ	Parallax (mas)	5.64 ± 0.10	2.925 ± 0.033	⋯	6.536 ± 0.047	$2.948^{+0.074}_{-0.075}$	$2.973^{+0.077}_{-0.076}$
d	Distance (pc)	$177.4^{+3.2}_{-3.1}$	$341.8^{+3.9}_{-3.8}$	⋯	153.0 ± 1.1	$339.2^{+8.8}_{-8.3}$	$336.4^{+8.9}_{-8.5}$
Planetary Parameters:							
P	Period (days)	$3.4095675^{+0.0000070}_{-0.0000069}$	5.0037775 ± 0.0000048	4.720219 ± 0.000011	10.180249 ± 0.000015	5.331751 ± 0.000011	5.331751 ± 0.000011
R_P	Radius (R_J)	$1.060^{+0.041}_{-0.034}$	$1.771^{+0.060}_{-0.056}$	$1.396^{+0.056}_{-0.054}$	$1.060^{+0.040}_{-0.039}$	$1.239^{+0.046}_{-0.039}$	$1.241^{+0.052}_{-0.049}$
M_P	Mass (M_J)	$6.33^{+0.29}_{-0.31}$	0.88 ± 0.16	2.37 ± 0.24	$0.851^{+0.052}_{-0.047}$	0.99 ± 0.11	$0.912^{+0.095}_{-0.10}$
T_0[i]	Optimal conjunction time ($\rm BJD_{TDB}$)	$2458629.47972 \pm 0.00039$	$2458459.73877^{+0.00071}_{-0.00083}$	$2458913.37033 \pm 0.00045$	$2458607.90338^{+0.00052}_{-0.00049}$	$2458990.55302^{+0.00081}_{-0.00079}$	$2458990.55306^{+0.00081}_{-0.00082}$
a	Semimajor axis (au)	$0.04860^{+0.00080}_{-0.00094}$	$0.06608^{+0.00098}_{-0.0011}$	$0.0626^{+0.0011}_{-0.0012}$	$0.0903^{+0.0018}_{-0.0013}$	$0.06864^{+0.00079}_{-0.00075}$	$0.06586^{+0.00069}_{-0.00075}$
i	Inclination (degrees)	$88.41^{+1.0}_{-0.93}$	$82.54^{+0.42}_{-0.59}$	$85.70^{+1.3}_{-0.65}$	$88.51^{+0.29}_{-0.22}$	$88.84^{+0.81}_{-1.1}$	$88.4^{+1.1}_{-1.3}$
e	Eccentricity	$0.072^{+0.021}_{-0.023}$	$0.050^{+0.054}_{-0.035}$	$0.073^{+0.092}_{-0.052}$	$0.024^{+0.032}_{-0.017}$	$0.036^{+0.044}_{-0.026}$	$0.057^{+0.050}_{-0.039}$

Table 4
(Continued)

Priors:		TOI-628 b	TOI-640 b	TOI-1333 b[a]	TOI-1478 b[b]	TOI-1601 b	
$\tau_{\rm circ}$	Tidal circularization timescale (Gyr)	$3.32^{+0.53}_{-0.61}$	$0.206^{+0.060}_{-0.057}$	$1.29^{+0.37}_{-0.33}$	$42.5^{+11}_{-8.1}$	1.85 ± 0.38	$1.52^{+0.42}_{-0.38}$
ω_*	Argument of periastron (degrees)	-74^{+13}_{-15}	159^{+86}_{-99}	105^{+64}_{-40}	-110^{+120}_{-130}	-180^{+110}_{-100}	120^{+57}_{-70}
$T_{\rm eq}$	Equilibrium temperature (K)	1586^{+52}_{-40}	1749^{+26}_{-30}	1679^{+35}_{-34}	918 ± 11	1619^{+24}_{-23}	1642^{+25}_{-24}
K	RV semiamplitude ($m\ s^{-1}$)	713^{+20}_{-22}	78 ± 14	223^{+22}_{-21}	$82.5^{+4.0}_{-3.8}$	$87.3^{+9.2}_{-9.9}$	$87.6^{+8.9}_{-9.6}$
R_P/R_*	Radius of planet in stellar radii	$0.08108^{+0.00075}_{-0.00071}$	$0.08738^{+0.00091}_{-0.00086}$	$0.0745^{+0.0014}_{-0.0015}$	0.1040 ± 0.0015	$0.05827^{+0.00071}_{-0.00070}$	$0.05834^{+0.00074}_{-0.00072}$
a/R_*	Semimajor axis in stellar radii	$7.78^{+0.22}_{-0.27}$	$6.82^{+0.22}_{-0.24}$	$6.98^{+0.24}_{-0.23}$	$18.54^{+0.70}_{-0.60}$	$6.76^{+0.17}_{-0.20}$	6.48 ± 0.23
Depth	Flux decrement at midtransit	0.00657 ± 0.00012	$0.00764^{+0.00016}_{-0.00015}$	0.00555 ± 0.00021	0.01083 ± 0.00032	$0.003395^{+0.000083}_{-0.000081}$	$0.003403^{+0.000087}_{-0.000083}$
τ	Ingress/egress transit duration (days)	$0.01247^{+0.0012}_{-0.00061}$	$0.0454^{+0.0028}_{-0.0026}$	$0.0177^{+0.0027}_{-0.0033}$	0.0208 ± -0.0022	$0.01483^{+0.00084}_{-0.00034}$	$0.01503^{+0.0013}_{-0.00049}$
T_{14}	Total transit duration (days)	$0.1576^{+0.0015}_{-0.0013}$	0.1502 ± 0.0017	$0.1934^{+0.0025}_{-0.0029}$	0.1736 ± 0.0023	0.2627 ± 0.0020	$0.2631^{+0.0022}_{-0.0021}$
b	Transit impact parameter	$0.23^{+0.13}_{-0.15}$	$0.8763^{+0.0063}_{-0.0067}$	$0.504^{+0.085}_{-0.19}$	$0.481^{+0.050}_{-0.076}$	$0.136^{+0.13}_{-0.095}$	$0.18^{+0.14}_{-0.12}$
$T_{S,14}$	Total eclipse duration (days)	$0.1387^{+0.0063}_{-0.0055}$	$0.1481^{+0.0070}_{-0.019}$	$0.208^{+0.041}_{-0.013}$	$0.1736^{+0.0075}_{-0.0066}$	$0.263^{+0.014}_{-0.013}$	$0.279^{+0.024}_{-0.017}$
ρ_P	Density (cgs)	$6.58^{+0.70}_{-0.75}$	$0.195^{+0.042}_{-0.040}$	$1.08^{+0.18}_{-0.15}$	$0.88^{+0.13}_{-0.11}$	$0.640^{+0.097}_{-0.093}$	$0.589^{+0.098}_{-0.091}$
$\log g_P$	Surface gravity	$4.145^{+0.031}_{-0.038}$	$2.841^{+0.078}_{-0.095}$	$3.479^{0.054}_{-0.056}$	$3.273^{+0.045}_{-0.043}$	$3.201^{+0.052}_{-0.059}$	$3.165^{+0.055}_{-0.061}$
T_S	Time of eclipse (BJD_{TDB})	$2458467.566^{+0.031}_{-0.038}$	$2454824.46^{+0.12}_{-0.20}$	$2458717.445^{+0.097}_{-0.13}$	$2455701.431^{+0.092}_{-0.12}$	$2454189.289^{+0.095}_{-0.17}$	$2454189.27^{+0.12}_{-0.19}$
$e \cos \omega_*$		$0.019^{+0.014}_{-0.018}$	$-0.012^{+0.038}_{-0.062}$	$-0.012^{+0.032}_{-0.042}$	$-0.002^{+0.014}_{-0.018}$	$-0.007^{+0.028}_{-0.049}$	$-0.013^{+0.035}_{-0.057}$
$e \sin \omega_*$		$-0.068^{+0.024}_{-0.022}$	$0.007^{+0.042}_{-0.029}$	$0.053^{+0.10}_{-0.056}$	$0.000^{+0.030}_{-0.029}$	$0.001^{+0.028}_{-0.027}$	$0.031^{+0.044}_{-0.033}$
d/R_*	Separation at midtransit	$8.29^{+0.36}_{-0.40}$	$6.76^{+0.38}_{-0.51}$	$6.59^{+0.54}_{-0.77}$	$18.58^{+0.97}_{-0.88}$	$6.74^{+0.32}_{-0.36}$	$6.27^{+0.41}_{-0.47}$

Notes. See Table 3 in Eastman et al. (2019) for a detailed description of all derived and fitted parameters.
[a] The SED was not included within the global fit for TOI-1333.
[b] No TESS dilution prior was used for TOI-1478 b because initial fits showed a fitted dilution past the 10% prior we used in the other systems. We fit for a dilution term within the fit for the TESS bandpass but with no prior.
[c] The tidal quality factor (Q_S) is assumed to be 10^6.
[d] T_C prior comes from analysis of the WASP photometry (see Section 2.2). We note that this time is in HJD_{TDB} while all data files and results here are BJD_{TDB}. The difference between these two time systems is on the order of seconds while the precision on T_C used as a prior is on order of minutes, and therefore has no influence on the results.
[e] We assume the TESS correction for blending is much better than 10%. We use a prior of 10% of the determined blending from TICv8 (Stassun et al. 2018).
[f] Dilution prior for TOI-1333 comes from our three-component SED analysis (see Section 2.6.4).
[g] The initial metallicity is the metallicity of the star when it was formed.
[h] The equal evolutionary point (EEP) corresponds to static points in a star's evolutionary history when using the MIST isochrones and can be a proxy for age. See Section 2 in Dotter (2016) for a more detailed description of EEP.
[i] Optimal time of conjunction minimizes the covariance between T_C and period. This is the transit midpoint.

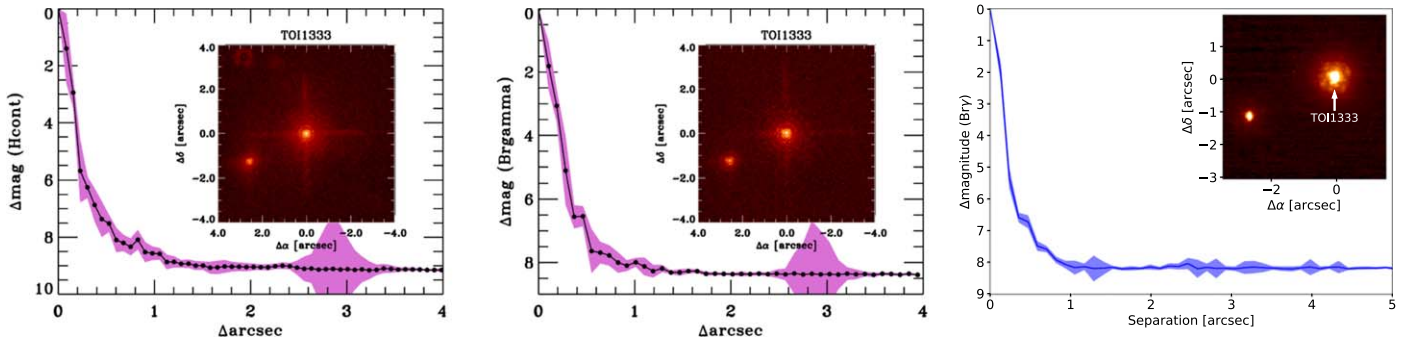

Figure 4. Palomar PHARO (left) H-band and (middle) Brγ-band 4σ contrast curve for TOI-1333 with the AO image embedded in the plot. The (right) Gemini NIRI Brγ-band AO 5σ contrast curve for TOI-1333. The NIRI AO image is embedded in the plot. The second star in the image is TIC 2010985858, and we properly account for its blending in our fit (see Section 3). The colored swath represents the uncertainty on the 5σ contrast curve (see Section 2.6.2).

and a pixel scale of 0.″033 pixel^{-1}. We conducted our observations using a square four-point dither pattern with a separation of 4″ between each dither position. Our observations were taken in natural guide-star mode with high winds. We obtained one sequence of observations in the *Ks* band and a second sequence in the *J* band for a total integration time of 510 s in the *Ks* band and 225 s in the *J* band. See Savel et al. (2020) for a detailed description of the observing strategy. Neither set of observations revealed any companions for TOI-628.

We observed TOI-1333 (Br–γ and $H-$cont) and TOI-1478 with infrared high-resolution adaptive optics (AO) imaging at Palomar Observatory. The Palomar Observatory observations were made with the PHARO instrument (Hayward et al. 2001) behind the natural guide-star AO system P3 K (Dekany et al. 2013). The observations were made on 2019 November 10 UT in a standard five-point quincunx dither pattern with steps of 5″. Each dither position was observed three times, offset in position from each other by 0.″5 for a total of 15 frames. The camera was in the narrow-angle mode with a full field of view of ∼25″ and a pixel scale of approximately 0.″025 per pixel. Observations were made in the narrow-band Br–γ filter ($\lambda_o = 2.1686$; $\Delta\lambda = 0.0326$ μm) for TOI-1333 and TOI-1478, and in the $H-$cont filter ($\lambda_o = 1.668$; $\Delta\lambda = 0.018$ μm) for TOI-1333. The observations get down to ΔMag = 6.54 (Br–γ) and 7.52 ($H-$cont) for TOI-1333 and ΔMag = 6.8 (Br–γ) for TOI-1478 (all at ∼0.″5).

TOI-1333 was also observed using NIRI on Gemini-North (Hodapp et al. 2003) on UT 2019 November 14 in the Br–γ filter. NIRI has a 22″ × 22″ field of view with a 0.″022 pixel scale. Our sequence consisted of nine images, each with exposure time 4.4 s, and we dithered the telescope between each exposure. A sky background was constructed from the dithered frames and subtracted from each science image. We also performed bad pixel removal and flat-fielding, and then aligned and coadded frames. NIRI got down to ΔMag = 6.7 at 0.″472.

We also observed TOI-1601 using the Near Infrared Camera 2 (NIRC2) AO setup on the W. M. Keck Observatory in the Br–γ filter and in the $J-$cont filter on UT 2020 September 9. The NIRC2 detector has a 9.971 mas pixel^{-1} using a 1024 × 1024 CCD (field of view = 10″ × 10″; Service et al. 2016). Unfortunately, the lower left quadrant of the CCD is known to have higher than typical noise levels in comparison to the others. To avoid this issue, a three-point dither pattern technique was used. The images were aligned and stacked after normal flat-field and sky background corrections. No nearby companions were seen down to Δmag = 6.680 ($J-$cont) and 6.402 (Br–γ) for TOI-1601 at 0.″5.

While the observing strategy differed, all of the AO data were processed and analyzed with a custom set of IDL tools. The science frames were flat-fielded and sky-subtracted. The flat fields were generated from a median combination of the dark-subtracted flats taken on sky. The flats were normalized such that the median value of the flats is unity. The sky frames were generated from the median average of the 15 dithered science frames; each science image was then sky-subtracted and flat-fielded. The reduced science frames were combined into a single combined image using an intrapixel interpolation that conserves flux, shifts the individual dithered frames by the appropriate fractional pixels, and median-coadds the frames (see Figure 4). The final resolution of the combined dither was determined from the FWHM of the point-spread function; the resolutions of the Br–γ and $H-$cont images are 0.″092 and 0.″075, respectively (Figure 4).

The sensitivities of the final combined AO images were determined by injecting simulated sources azimuthally around the primary target every 20° at separations of integer multiples of the central source's FWHM (Furlan et al. 2017; M. Lund et al. 2021, in preparation). The brightness of each injected source was scaled until standard aperture photometry detected it with 5σ significance. The resulting brightness of the injected sources relative to the target set the contrast limits at that injection location. The final 5σ limit at each separation was determined from the average of all of the determined limits at that separation, and the uncertainty on the limit was set by the rms dispersion of the azimuthal slices at a given radial distance. The sensitivity curves for TOI-1333 are shown in Figure 4 along with an inset image zoomed in to the primary target showing no other companion stars.

2.6.3. TOI-1333 Companions

In the case of TOI-1333, two additional sources were detected in the PHARO and GEMINI AO imaging (Figure 4; only the 3″ companion is shown). The first source is 7.″43 (Gaia Collaboration et al. 2018) to the east of the primary target and is separately resolved by the Two Micron All Sky Survey (2MASS J21400422+4824221; TIC 395171213). The second source is only 2.″81 (Gaia Collaboration et al. 2018) away and was not separately detected by 2MASS, although it was detected by Gaia and hence is in the TESS Input Catalog (TIC 2010985858). Based on the differential magnitudes measured by Palomar, the deblended infrared magnitudes for the primary

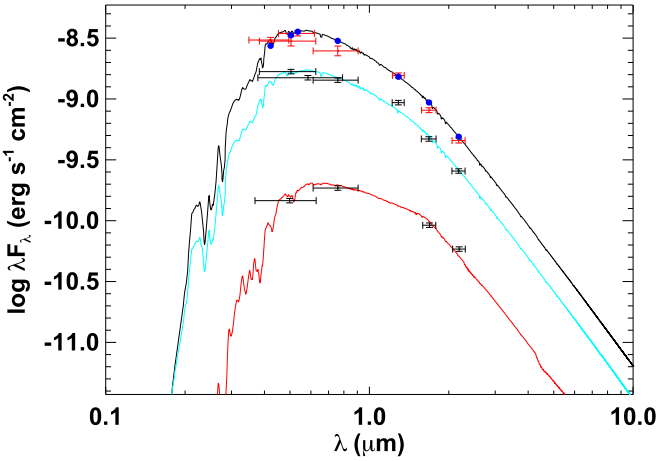

Figure 5. Three-component SED fit for TOI-1333. The blue points are the predicted integrated fluxes for the primary star. The red and black points are the observed values at the corresponding passbands for each star. The widths of the passbands are the horizontal error bars, and the vertical errors represent the 1σ uncertainties. The final model fit is shown by the solid line for TOI-1333 (black) and the 7″ (cyan) and bound 3″ (red) companions.

star and nearby companion are $K_1 = 8.355 \pm 0.024$ mag, $H_1 = 8.514 \pm 0.043$ mag ($H_1 - K_1 = 0.159 \pm 0.049$) and $K_2 = 10.614 \pm 0.026$ mag, $H_2 = 10.871 \pm 0.044$ mag ($H_2 - K_2 = 0.257 \pm 0.051$), respectively. The 3″ star has a Gaia magnitude of $G = 12.6221 \pm 0.0016$.

The primary target has a Gaia distance of 200.5 ± 1.2 pc, whereas the 7″ companion has a Gaia distance of 1030 ± 35 pc, indicating that this companion is not bound to the primary and is simply a chance alignment near the line of sight to TOI-1333. However, the 3″ companion has a Gaia distance of 196.8 ± 1.6 pc and proper motions that are nearly identical to that of the primary star ($\mu 1_\alpha = -9.81 \pm 0.05$ versus $\mu 2_\alpha = -9.06 \pm 0.08$ and $\mu 1_\delta = -10.50 \pm 0.04$ versus $\mu 2_\delta = -9.24 \pm 0.12$ mas/yr); it is, therefore, highly probable that TIC 2010985858 is physically bound to the primary star with a projected separation of ∼590 au. We account for the blended light from these two companions in our global analysis (see Section 3 for details on how).

We use the LOFTI software package (Pearce et al. 2020) to derive orbital parameters of the visual binary system formed by TOI-1333 and its companion. LOFTI uses the relative proper motions of the two stars from the Gaia catalog to sample probable orbits for a binary star system. To derive the mass of the companion—required to fit the orbit using LOFTI—we use the `isochrones` package (Morton 2015). We perform a spectral energy distribution (SED) fit on photometry from TOI 1333's binary companion using the Gaia G, BP, and RP magnitudes, along with its Gaia parallax. Using the MESA Isochrones and Stellar Tracks (MIST) isochrone (Dotter 2016) as the base isochrone, we derive a mass for the companion of $0.808^{+0.043}_{-0.042}\ M_\odot$. We use the astrometric parameters for the two systems from Gaia EDR3.

The LOFTI fit reveals that the semimajor axis of the binary orbit is 570^{+590}_{-170} au and the orbital inclination is 125^{+18}_{-10} degrees, ruling out an edge-on orbit for the binary at high confidence. The orbital eccentricity is weakly constrained to be less than 0.69 with 95% confidence (with a slight preference for values between 0.5 and 0.7, but consistent with zero). An independent analysis of TOI-1333 and its companion were presented in Mugrauer & Michel (2020).

2.6.4. TOI-1333 Spectral Energy Distribution

The presence of the two stellar companions within a few arcseconds of TOI-1333 implies that the TESS and SG1 light curves of the TOI-1333 planet transit are likely to be diluted to some extent by the light from these other stars. Although the QLP corrects the TESS light curve for the blended contributions of known targets in the TESS input catalog (TIC), we need to correct the follow-up photometry from TFOP for different amounts of dilution. To quantify this flux dilution, we performed a multicomponent SED fit with Kurucz model atmospheres following the procedures described in Stassun & Torres (2016), utilizing the resolved broadband measurements from Gaia, 2MASS, and our AO observations (see Section 2.6.2).

We adopted the spectroscopic $T_{\rm eff}$ (6250 ± 100 K) from TRES for TOI-1333 and the $T_{\rm eff}$ from the TICv8 (Stassun et al. 2019) and from the Gaia DR2 catalog for the companions, with A_V being left as a free parameter but limited to the maximum line-of-sight value from the dust maps of Schlegel et al. (1998). The resulting fits are shown in Figure 5, with best-fit $A_V = 0.06 \pm 0.06$ for the TOI-1333 planet host. Integrating the SED models over the TESS bandpass gives the total flux dilution $(F_2 + F_3)/F_1 = 0.55$ with values of 0.56 in the I band, 0.54 in the R band, and 0.58 in the Sloan z'. We also used the SED fits to constrain the contribution from only the 2″ companion since some of our follow-up photometry only resolved the 7″ companion. The flux dilution of F_2/F_1 is 0.07 in the I band, 0.06 in the R band, and 0.07 in the Sloan z'. By combining the deblended SED of the primary star TOI-1333 with the known Gaia DR2 parallax, we measure its radius to be $R_\star = 1.963 \pm 0.064\ R_\odot$. We use this as a prior on the global fit for TOI-1333 (see Section 3).

2.7. Location in the Galaxy, UVW Space Motion, and Galactic Population

For each of the TOIs analyzed here, we used their parallaxes, proper motions, and radial velocities and associated uncertainties from the Gaia DR2 catalog (Gaia Collaboration et al. 2018) to determine their location, kinematics, orbits, and associations with known stellar populations.[78] We corrected the native DR2 parallaxes and uncertainties using the prescription given in Lindegren et al. (2018). From these we computed the *prior* (DR2-based) estimates of the distances to the systems.[79] We used these to compute the heliocentric UVW space motions of the host stars, and then corrected for the Sun's motion $(UVW)_\odot$ with respect to the local standard of rest (LSR) as determined by Coşkunoğlu et al. (2011). These resulting (UVW) values are shown in Table 1. We note that we adopt a right-handed coordinate system, such that a positive U is toward the Galactic center.

We used the Galactic latitudes and distances to the systems to estimate their Z height relative to the Sun, and then corrected for the $Z_\odot \simeq 30$ pc offset of the Sun from the Galactic plane as determined by Bovy (2017) from the analysis of local giants. We use the UVW velocities relative to the LSR to determine the likelihood that the star belongs to a thin disk, thick disk, halo, or Hercules stream,[80] using the categorization scheme of

[78] We acknowledge that some of the analysis in this section was inspired by and follows that of Burt et al. (2020).

[79] We note that, for self-consistency, we explicitly did not adopt the *posterior* values of the parallaxes from the global fit as listed in Table 4.

[80] The Hercules stream is a chemically heterogeneous population of nearby stars that have distinct kinematics relative to the bulk of the local stellar distribution. See, for example, Bensby et al. (2007).

Bensby et al. (2014). We also report the estimates of the parameters of the Galactic orbits of the systems as determined by Mackereth & Bovy (2018) using Gaia DR2 astrometry and radial velocities.[81] We estimated the spectral type of each TOI using its $T_{\rm eff}$ as determined from the global fit and given in Table 4 and using the $T_{\rm eff}$–spectral type relations of Pecaut & Mamajek (2013). We then compared the position and orbits of the systems to the scale height h_Z of stars of similar spectral type as determined by Bovy (2017).

Finally, we also consider whether the systems may belong to any of the known nearby ($\lesssim$150 pc), young ($\lesssim$Gyr) associations using the BANYAN Σ (Bayesian Analysis for Nearby Young AssociatioNs Σ) estimator (Gagné et al. 2018). Not surprisingly, none of the systems had any significant ($\gtrsim$1%) probability of being associated with these young associations, and the BANYAN Σ estimator assigned all five systems as belonging to the "field" with a high probability $\gtrsim$99%. We now discuss the results for each of the systems individually.

TOI-628: We find a distance from the Sun of $d = 178 \pm 3$ pc, consistent with the *posterior* value listed in Table 4, and $Z - Z_\odot \simeq -23$ pc. We derive velocities relative to the LSR of $(U, V, W) = (-8.7 \pm 0.4, 3.2 \pm 0.2, 4.2 \pm 0.1)$ km s^{-1}. According to the categorization scheme of Bensby et al. (2014), the system has a >99% probability of belonging to the thin disk. The Galactic orbit as estimated by Mackereth & Bovy (2018) has a perigalacticon of $R_p = 7.67$ kpc and apogalacticon of $R_a = 8.19$ kpc, an eccentricity of $e = 0.03$, and a maximum Z excursion from the Galactic plane of $Z_{\rm max} = 63$ pc. This orbit is consistent with both the current location of the system and the scale height of 97 pc for stars of similar spectral type (F7V). Indeed, TOI-628 is relatively dynamically "cold" for its spectral type. In other words, it has an orbit that is fairly close to that of the local LSR.

TOI-640: We find a distance from the Sun of $d = 340 \pm 4$ pc, consistent with the *posterior* value listed in Table 4, and $Z - Z_\odot \simeq -76$ pc. We derive velocities relative to the LSR of $(U, V, W) = (-16.8 \pm 0.2, -16.7 \pm 0.4, -8.7 \pm 0.2)$ km s^{-1}. According to the categorization scheme of Bensby et al. (2014), the system has an ∼99% probability of belonging to the thin disk. The Galactic orbit as estimated by Mackereth & Bovy (2018) has a perigalacticon of $R_p = 6.28$ kpc and apogalacticon of $R_a = 8.16$ kpc, an eccentricity of $e = 0.13$, and a maximum Z excursion from the Galactic plane of $Z_{\rm max} = 150$ pc. This orbit is both consistent with the current location of the system and suggests that the system is nearing its maximum excursion above the plane. It is also consistent with the scale height of 85 pc for stars of similar spectral type (F5.5V).

TOI-1333: We find a distance from the Sun of $d = 200 \pm 2$ pc and $Z - Z_\odot \simeq 19$ pc. We derive velocities relative to the LSR of $(U, V, W) = (23.0 \pm 0.1, -1.00 \pm 0.3, -6.0 \pm 0.1)$ km s^{-1}. According to the categorization scheme of Bensby et al. (2014), the system has an ∼99% probability of belonging to the thin disk. The Galactic orbit as estimated by Mackereth & Bovy (2018) has a perigalacticon of $R_p = 7.25$ kpc and apogalacticon of $R_a = 8.32$ kpc, an eccentricity of $e = 0.07$, and a maximum Z excursion from the Galactic plane of $Z_{\rm max} = 91$ pc. This orbit is consistent with the current location of the system. It is also consistent with the scale height of 97 pc for stars of similar spectral type (F7V).

TOI-1478: We find a distance from the Sun of $d = 153 \pm 1$ pc, and $Z - Z_\odot \simeq 67$ pc. We derive velocities relative to the LSR of $(U, V, W) = (-37.0 \pm 0.3, 26.4 \pm 0.4, 32.5 \pm 0.2)$ km s^{-1}. According to the categorization scheme of Bensby et al. (2014), the system has an ∼88% probability of belonging to the thin disk and an ∼12% probability of belonging to the thick disk (and negligible probabilities of belonging to the halo or Hercules stream). The Galactic orbit as estimated by Mackereth & Bovy (2018) has a perigalacticon of $R_p = 7.71$ kpc and apogalacticon of $R_a = 10.34$ kpc, an eccentricity of $e = 0.14$, and a maximum Z excursion from the Galactic plane of $Z_{\rm max} = 650$ pc. Unfortunately, Bovy (2017) was unable to determine the scale height of stars of similar spectral type (G6V), due to incompleteness. Nevertheless, it would appear that TOI-1478's orbit has a maximum Z excursion that exceeds the expected scale height for stars of similar spectral type as estimated by extrapolating from the results of Bovy (2017) from earlier spectral types. Surprisingly, its current distance above the plane is only a small fraction of its predicted maximum excursion. In summary, the weight of evidence suggests that TOI-1478 may well be a thick disk star that we happen to be observing when it is near the Galactic plane. Detailed chemical abundance measurements (e.g., [α/Fe]) may provide corroborating evidence for or against this hypothesis.

TOI-1601: We find a distance from the Sun of $d = 336 \pm 9$ pc, consistent with the *posterior* value listed in Table 4, and $Z - Z_\odot \simeq -73$ pc. We derive velocities relative to the LSR of $(U, V, W) = (-8.1 \pm 0.7, -14.5 \pm 0.7, 20.9 \pm 0.4)$ km s^{-1}. According to the categorization scheme of Bensby et al. (2014), the system has an ∼98% probability of belonging to the thin disk. The Galactic orbit as estimated by Mackereth & Bovy (2018) has a perigalacticon of $R_p = 6.50$ kpc and apogalacticon of $R_a = 8.32$ kpc, an eccentricity of $e = 0.12$, and a maximum Z excursion from the Galactic plane of $Z_{\rm max} = 351$ pc. This orbit is consistent with the current location of the system. The maximum Z excursion is a factor of ∼3.3 times larger than the scale height of 103 pc for stars of similar spectral type (G0V). The probability that a star in a population with a given scale height $h_z = 108$ pc has a maximum excursion of $z_{\rm max} = 351$ pc is nonnegligible. Thus, we expect that TOI-1601 is a thin disk star that is simply in the tail of the distribution of $z_{\rm max}$. Again, detailed abundances could corroborate or refute this conclusion.

3. EXOFASTv2 Global Fits

We use the publicly available exoplanet fitting suite, `EXOFASTv2` (Eastman et al. 2013, 2019), to globally fit the available photometry and RVs to determine the host star and planetary parameters for TOI-628 b, TOI-640 b, TOI-1333 b, TOI-1478 b, and TOI-1601 b. We fit the TESS and SG1 transits (see Section 2.4), accounting for the 30 minute smearing from the FFIs. Within the fit, the SG1 light curves were detrended (additive) against the corresponding parameters shown in Table 1. See Section D in the appendix of Collins et al. (2017) for a description of each detrending parameter. We use the MIST stellar evolution models (Paxton et al. 2011, 2013, 2015; Choi et al. 2016; Dotter 2016) and the SED within the fit to determine the host star parameters for

[81] We note that Mackereth & Bovy (2018) adopted a solar Galactocentric distance of $R_0 = 8$ kpc, $Z_\odot = 25$ pc, and a local circular velocity of $V_{\rm circ} = 220$ km s^{-1}. They also corrected for the Sun's motion with respect to the LSR using the values of $(UVW)_\odot$ determined by Schönrich et al. (2010), which differ slightly from the values we adopted as determined by Coşkunoğlu et al. (2011). However, this is a minor effect and has no qualitative impact on our conclusions.

all systems but TOI-1333 b. The SED fit within the global fit puts systematic floors on the broadband photometry errors (see Table 1; Stassun & Torres 2016). We also note that EXOFASTv2 defaults to a lower limit on the systematic error on the bolometric flux ($F_{\rm bol} \sim 3\%$) given the spread seen from various techniques to calculate it (Zinn et al. 2019). We place a Gaussian prior on the metallicity from our analysis of the host star's spectra from TRES, or CHIRON in the case of TOI-640 (see Sections 2.5.3 and 2.5.2). We also place a Gaussian prior on the parallax from Gaia (Gaia Collaboration et al. 2016, 2018), correcting for the 30 μas offset reported by Lindegren et al. (2018), and an upper limit on the line-of-sight extinction from Schlegel et al. (1998) and Schlafly & Finkbeiner (2011). We also fit for a dilution term on the TESS band. Since the QLP corrects the TESS light curves for all known blended companions, we place a Gaussian prior of $0\% \pm 10\%$ of the contamination ratio reported by the TIC (Stassun et al. 2018). We assume that the light curve has been corrected to a precision better than 10% (and test this with preliminary EXOFASTv2, showing the dilution to be consistent with zero), but this flexibility also provides an independent check on the correction applied and allows us to propagate the uncertainty in the correction. We do not find any significant additional dilution in any of the systems (within this prior and consistent with zero dilution) other than TOI-1478 b, where our fit suggests an additional 13% dilution ($0.126^{+0.020}_{-0.021}$) is needed for the TESS light curve to be consistent with the TFOP photometry. For this fit, we remove this prior, essentially allowing the TFOP observations to constrain the depth of the transit. The cause of this additional dilution is not clear since we see no evidence for any unknown companions in our high-spatial-resolution imaging. We note that TESS only observed three transits in one sector for TOI-1478 b, the longest-period planet in our sample, and the TFOP light curves were both at higher spatial resolution. We also ran a fit where we allowed for a slope in the RVs, but we found no significant trends for any system (we do not fit for a slope in the final fits). A list of the priors for each target is shown in Table 4. Table 3 of Eastman et al. (2019) shows a list and description of the fitted and derived parameters, including the bounds that EXOFASTv2 adopts for each fitted parameter. We note that eccentricity, a key parameter for this study, is bound as such, $0 \leqslant e \leqslant 1 - \frac{a + R_p}{R_*}$, in order to ensure that the periastron values of the planet orbits are larger than the sum of the stellar and planetary radius. We deem a fit to be fully converged by following the recommended statistical threshold of a Gelman–Rubin statistic (<1.01) and the independent draw (>1000) that is recommended by Eastman et al. (2019). The results from our EXOFASTv2 fits are shown in Tables 4 and 5, and the models are shown for the transits and RVs in Figures 2 and 3.

In the case of TOI-1333 b, we deviate slightly from the methodology in the previous paragraph because there are two nearby bright companions, both detected by high-resolution imaging (see Section 4). The 2″ nearby companion and 7″ star were blended in the TESS and CRCAO photometry (see Section 2.4), but only the 2″ companion was blended in the LCO observations. While the TESS light curve has already been deblended as part of the reduction pipeline (see Section 2.1), the SG1 observations were not. Our three-component SED analysis (see Section 2.6.4) determined that the nearby companion 2″ from TOI-1333 accounts for 6.6% in the z'band, where LCO did not resolve the close companion. The combined flux contribution from both stars is 36.1% in the I band and 35.0% in the R band, where both companions were unresolved by CRCAO. We use these values with a 5% Gaussian prior EXOFASTv2 global fit (also placing the prior on the TESS dilution as discussed in the previous paragraph). We place a Gaussian prior on the host star's radius from the SED analysis of $R_\star = 1.963 \pm 0.064\ R_\odot$. Preliminary SED fits of TOI-1333 using EXOFASTv2 and independent $\log g$ constraints from the SPC analysis of the TRES spectra suggested that TOI-1333 is a slightly evolved star. Given that the SED would normally constrain the $T_{\rm eff}$ of the host star within the fit but was excluded for TOI-1333, we also place a prior on the $T_{\rm eff}$ of 6250 ± 100 K from the SPC analysis of the TRES spectroscopy.

For TOI-1478 global fit, five RVs were acquired in the summer and winter of 2020, after a multimonth shutdown due to the COVID-19 pandemic. When included as part of the CHIRON RVs in the fit, we see a statistically significant slope measured of 0.176 m s^{-1} day^{-1}. However, the RV baseline for CHIRON observations has appeared to shift slightly when pre- and postshutdown RVs were compared for standard stars, consistent with the shift we measured when including these postpandemic RVs (T. Henry 2021, private communication). Since we saw no evidence of a slope in fits without these RVs and we know there is a shift observed in the RV baseline for CHIRON, we treat these observations as a separate instrument (labeled "CHIRON2"). When fitting the CHIRON RVs separately within the EXOFASTv2 fit, we see a difference of 65 m s^{-1} in the fitted RV zero-points. We note that the planet and host star parameters are consistent to $<1\sigma$ whether or not this slope is included in the fit.

3.1. TOI-1601 Bimodality

After each EXOFASTv2 fit, we inspect the posteriors of each fitted and derived parameter, visually inspecting for any anomalies such as multimodal distributions. In all cases but TOI-1601 b, no issues were noted. For TOI-1601 b, we see a clear bimodal distribution in the mass and age of the host star (see Figure 6). We find two peaks in the mass distribution at 1.340 and 1.517 $M_\odot$, which correspond to the two peaks seen in the age distribution at 4.27 and 2.63 Gyr. There is no optimal way to represent the bimodal solution, so we split the mass of the host star at the minimum value of 1.415 $M_\odot$ and extract two solutions for both peaks identified. We adopt the high-mass solution for the discussion since it has a higher probability (66.7%) of being correct from our analysis, but we present both solutions in Table 4 for future analysis. We note that we observed no significant change in any systematic parameters, suggesting the bimodality is due to our limited precision that is not sufficient to completely separate similar solutions, due to the host star being slightly evolved.

4. Discussion

These five newly discovered hot Jupiters from NASA's TESS mission significantly increase (>5%) the number of well-characterized (measured masses and orbital eccentricities) giant planets that reside in orbits with periods between 5 and 15 days, a regime where planets experience weaker tidal forces than those experienced by planets closer to their host stars and, as a result, are not likely to have had enough time to circularize

Table 5
Median Values and 68% Confidence Intervals for the Global Models

TOI-628						
Wavelength Parameters:		B	r'	z'	TESS	
u_1	Linear limb-darkening coeff	$0.646^{+0.058}_{-0.061}$	0.329 ± 0.051	$0.213^{+0.053}_{-0.052}$	$0.236^{+0.045}_{-0.046}$	
u_2	Quadratic limb-darkening coeff	0.286 ± 0.057	0.306 ± 0.049	0.313 ± 0.050	$0.292^{+0.047}_{-0.048}$	
A_D	Dilution from neighboring stars	⋯	⋯	⋯	0.0012 ± 0.0036	
Telescope Parameters:		MINERVAF3	MINERVAF4	MINERVAF6	TRES	
$\gamma_{\rm rel}$	Relative RV offset ($m\ s^{-1}$)	19990^{+26}_{-28}	19969 ± 35	20032^{+26}_{-25}	-633^{+20}_{-18}	
σ_J	RV Jitter ($m\ s^{-1}$)	60^{+29}_{-18}	102^{+36}_{-24}	83^{+26}_{-20}	54^{+28}_{-20}	
σ_J^2	RV Jitter variance	3700^{+4400}_{-1800}	10400^{+8600}_{-4300}	7000^{+4900}_{-2900}	2900^{+3800}_{-1700}	
Transit Parameters:		TESS	KeplerCam UT 2019-12-06 (z')	LCO SSO UT 2019-12-16 (B)	Whitin UT 2020-02-08 (r')	
σ^2	Added variance	$0.000000119^{+0.000000024}_{-0.000000020}$	$0.0000366^{+0.0000020}_{-0.0000018}$	$0.00001138^{+0.0000010}_{-0.00000091}$	$0.00000765^{+0.00000047}_{-0.00000044}$	
F_0	Baseline flux	$0.999998^{+0.000039}_{-0.000038}$	0.99958 ± 0.00023	1.00071 ± 0.00021	1.00125 ± 0.00012	
C_0	Additive detrending coeff	⋯	⋯	$0.00806^{+0.00058}_{-0.00057}$	-0.00277 ± 0.00031	
TOI-640						
Wavelength Parameters:		I	z'	TESS	V	
u_1	Linear limb-darkening coeff	0.191 ± 0.051	0.170 ± 0.036	0.216 ± 0.046	0.376 ± 0.050	
u_2	Quadratic limb-darkening coeff	0.311 ± 0.049	0.313 ± 0.035	0.314 ± 0.046	0.329 ± 0.049	
A_D	Dilution from neighboring stars	⋯	⋯	0.0000 ± 0.0022	⋯	
Telescope Parameters:		CHIRON				
$\gamma_{\rm rel}$	Relative RV offset ($m\ s^{-1}$)	$39091^{+10.}_{-11}$				
σ_J	RV Jitter ($m\ s^{-1}$)	$32.3^{+12}_{-8.3}$				
σ_J^2	RV Jitter variance	1040^{+900}_{-470}				
Transit Parameters:		TESS	Brierfield UT 2019-12-27 (I)	PEST UT 2020-03-01 (V)	LCO SSO UT 2020-08-23 (z')	LCO SSO UT 2020-11-06 (z')
σ^2	Added variance	$-0.0000000009^{+0.0000000093}_{-0.0000000081}$	$0.00000259^{+0.00000059}_{-0.00000051}$	$0.00000220^{+0.00000052}_{-0.00000045}$	$0.00000187^{+0.00000053}_{-0.00000041}$	$0.000000056^{+0.000000098}_{-0.000000080}$
F_0	Baseline flux	1.000016 ± 0.000022	0.99995 ± 0.00018	0.99984 ± 0.00019	0.99956 ± 0.00023	1.00034 ± 0.00012
C_0	Additive detrending coeff	⋯	-0.0183 ± 0.0033	⋯	$0.00080^{+0.00050}_{-0.00049}$	-0.00052 ± 0.00025
C_1	Additive detrending coeff	⋯	-0.0233 ± 0.0033	⋯	⋯	⋯
TOI-1333						
Wavelength Parameters:		I	R	z'	TESS	
u_1	Linear limb-darkening coeff	0.228 ± 0.049	0.258 ± 0.046	0.183 ± 0.035	$0.226^{+0.043}_{-0.044}$	
u_2	Quadratic limb-darkening coeff	0.323 ± 0.049	0.297 ± 0.048	0.303 ± 0.035	0.306 ± 0.047	

Table 5
(Continued)

A_D	Dilution from neighboring stars	0.345 ± 0.016	0.344 ± 0.017	0.0671 ± 0.0033	-0.016 ± 0.028		
Telescope Parameters:		TRES					
$\gamma_{\rm rel}$	Relative RV offset (m s^{-1})	122^{+15}_{-14}					
σ_J	RV Jitter (m s^{-1})	41^{+21}_{-18}					
σ_J^2	RV Jitter variance	1700^{+2100}_{-1200}					
Transit Parameters:		TESS	CRCAO UT 2020-07-29 (I)	LCO McD UT 2020-07-29 (z')	LCO McD UT 2020-08-12 (z')	CRCAO UT 2020-09-19 (R)	
σ^2	Added variance	$0.000000175^{+0.000000026}_{-0.000000023}$	$0.00000078^{+0.00000014}_{-0.00000012}$	$0.00000732^{+0.0000011}_{-0.00000097}$	$0.00000353^{+0.00000052}_{-0.00000046}$	$0.000000883^{+0.000000092}_{-0.000000084}$	
F_0	Baseline flux	0.999984 ± 0.000036	0.99985 ± 0.00012	$0.99927^{+0.00024}_{-0.00025}$	1.00245 ± 0.00018	1.00015 ± 0.00012	
C_0	Additive detrending coeff	⋯	0.00033 ± 0.00023	-0.00060 ± 0.00065	$0.01022 \pm$, 0.00068	$-0.00017^{+0.00021}_{-0.00022}$	
TOI-1478							
Wavelength Parameters:		R	i'	TESS			
u_1	Linear limb-darkening coeff	0.408 ± 0.048	0.349 ± 0.044	0.410 ± 0.045			
u_2	Quadratic limb-darkening coeff	0.258 ± 0.049	0.264 ± 0.047	$0.320^{+0.048}_{-0.047}$			
A_D	Dilution from neighboring stars	⋯	⋯	$0.126^{+0.020}_{-0.021}$			
Telescope Parameters:		CHIRON1	CHIRON2	CORALIE	FEROS	TRES	
$\gamma_{\rm rel}$	Relative RV offset (m s^{-1})	19384.9 ± 7.0	19419 ± 11	$20833.5^{+5.2}_{-5.4}$	20821.5 ± 4.5	-30 ± 12	
σ_J	RV Jitter (m s^{-1})	$32.3^{+6.6}_{-5.5}$	$1.5^{+37}_{-1.5}$	$0.00^{+13}_{-0.00}$	$10.4^{+4.2}_{-4.5}$	$20.1^{+1.7}_{-3.3}$	
σ_J^2	RV Jitter variance	1040^{+470}_{-320}	0^{+1500}_{-300}	-7^{+180}_{-91}	108^{+110}_{-74}	405^{+69}_{-120}	
Transit Parameters:		TESS	KeplerCam UT 2019-12-14 (i')	PEST UT 2020-01-03 (R)			
σ^2	Added variance	$0.000000083^{+0.000000049}_{-0.000000039}$	$0.00000537^{+0.00000039}_{-0.00000036}$	$0.0000136^{+0.0000012}_{-0.0000011}$			
F_0	Baseline flux	1.000054 ± 0.000061	1.00003 ± 0.00016	1.00026 ± 0.00022			
C_0	Additive detrending coeff	⋯	0.00146 ± 0.00035	⋯			
TOI-1601							
Wavelength Parameters:		I	R	z'	TESS		
u_1	Linear limb-darkening coeff	0.281 ± 0.050	0.285 ± 0.050	0.215 ± 0.047	0.305 ± 0.045		
u_2	Quadratic limb-darkening coeff	$0.305^{+0.050}_{-0.049}$	$0.260^{+0.049}_{-0.050}$	$0.281^{+0.049}_{-0.048}$	0.297 ± 0.048		
A_D	Dilution from neighboring stars	⋯	⋯	⋯	-0.0005 ± 0.0047		
Telescope Parameters:		TRES					
$\gamma_{\rm rel}$	Relative RV offset (m s^{-1})	$-100.8^{+7.0}_{-7.3}$					
σ_J	RV Jitter (m s^{-1})	$0.00^{+21}_{-0.00}$					
σ_J^2	RV Jitter variance	-110^{+540}_{-300}					
Transit Parameters:		TESS	GMU UT 2020-08-30 (R)	GMU UT 2020-09-15 (R)	CRCAO UT 2020-10-01 (R)	Adams UT 2020-10-17 (I)	LCO McD UT 2020-10-17 (z')

Table 5
(Continued)

σ^2	Added variance	$-0.000000044^{+0.000000024}_{-0.000000020}$	$0.00001324^{+0.0000010}_{-0.00000097}$	$0.0000105^{+0.0000020}_{-0.0000017}$	$0.00000134^{+0.00000025}_{-0.00000021}$	$0.00000066^{+0.00000017}_{-0.00000015}$	$0.00000069^{+0.00000016}_{-0.00000014}$
F_0	Baseline flux	0.999969 ± 0.000042	0.99318 ± 0.00018	1.00037 ± 0.00032	1.00043 ± 0.00012	1.00036 ± 0.00011	$0.998577^{+0.000091}_{-0.000092}$
C_0	Additive detrending coeff	⋯	-0.01148 ± 0.00042	-0.015 ± 0.010	-0.00039 ± 0.00033	-0.00232 ± 0.00034	-0.00039 ± 0.00024
C_1	Additive detrending coeff	⋯	0.00226 ± 0.00067	0.018 ± 0.010	⋯	-0.00638 ± 0.00063	-0.0015 ± 0.0013
C_2	Additive detrending coeff	⋯	⋯	-0.00160 ± 0.00053	⋯	⋯	⋯

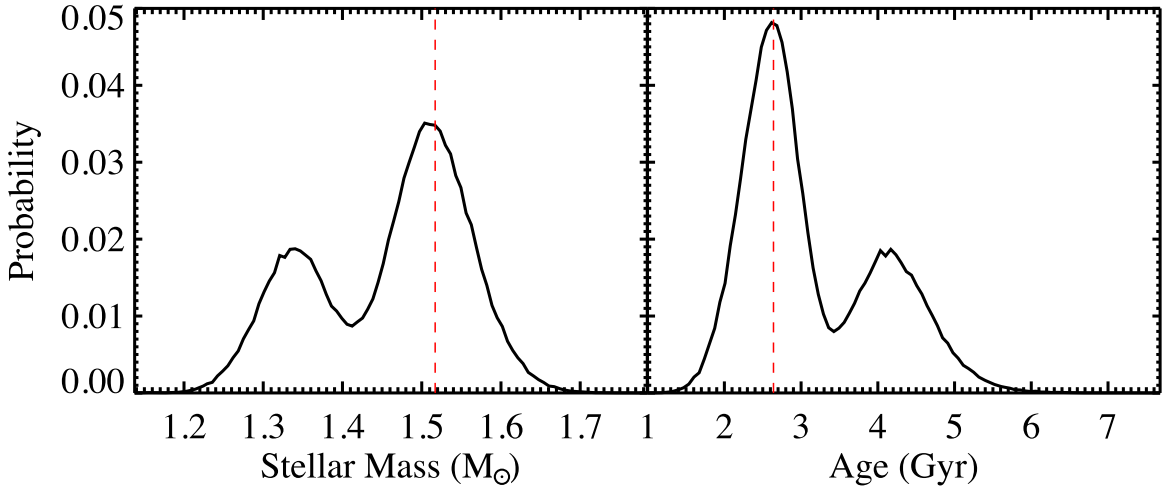

Figure 6. The (left) $M_{\rm star}$ and (right) age probability distribution function for TOI-1601 from our global fit. We split this panel at the valley of $M_* = 1.415\ M_\odot$ and extract two separate solutions, one for each of the peaks in the posteriors (see Table 4). The red line shows the median value for each parameter from the higher-mass solution with a probability of 68.4% (see Section 3).

their orbits. Additionally, these longer-period systems enable us to explore the "reinflation" scenario, an area where TESS should make a huge impact given its high photometric precision. By continuing to discover and characterize new giant planets at longer periods, we can look for evidence (through their eccentricity distribution) of the dominant migration mechanism. Additionally, TESS will provide a complete magnitude-limited sample of hot Jupiters ($P < 10$ days, Zhou et al. 2019), allowing us to test whether multiple populations exist within the distribution of key parameters (mass, radius, eccentricity), where some tentative trends have been suggested (Nelson et al. 2017; Ikwut-Ukwa et al. 2021). Here we provide a short overview of our global fit results on each of the five new systems. We note that all three of the planets found to be orbiting subgiant host stars (TOI-640, TOI-1333, and TOI-1601) reside in circular orbits.

4.1. TOI-628 b

TOI-628 (TIC 281408474) is a $V = 10.18$ late-F star with a mass of $M_* = 1.311^{+0.066}_{-0.075}\ M_\odot$, radius of $R_* = 1.345^{+0.046}_{-0.040}\ R_\odot$, and an age of $1.28^{+1.6}_{-0.91}$ Gyr. Its planetary companion (TOI-628 b) has a radius of $R_{\rm P} = 1.060^{+0.041}_{-0.034}\ R_{\rm J}$ and a mass of $M_{\rm P} = 6.33^{+0.29}_{-0.31}\ M_{\rm J}$ and is on a 3.4096 day period orbit. Our global analysis measures a nonzero orbital eccentricity of $e = 0.072^{+0.021}_{-0.023}$. Within our global fit, we derive a circularization timescale of $\tau_{\rm circ} = 3.32^{+0.53}_{-0.61}$ Gyr (for this system, assuming equilibrium tides and tidal quality factors for the planet and star of $Q_p\ 10^6$ and $Q_*\ 10^6$; Adams & Laughlin 2006) for this system, which is longer than our estimated age from MIST of $1.28^{+1.6}_{-0.91}$ Gyr. Thus the small but nonzero eccentricity is likely a vestige of the initially high eccentricity that the planet obtained during some process that initiated high-eccentricity migration, a high eccentricity that was subsequently damped to the eccentricity we see today. Without a tighter constraint on the system's age, this is not conclusive. Also of interest is the high mass of TOI-628 b, which makes it one of only a few dozen known hot Jupiters with a mass $>6\ M_{\rm J}$, and the most massive hot Jupiter found from TESS to date (see Figure 7).

4.2. TOI-640 b

The host star TOI-640 (TIC 147977348) is an F-star with a mass of $1.526^{+0.072}_{-0.079}\ M_\odot$ and a radius of $2.082^{+0.064}_{-0.058}\ R_\odot$. The host star appears to be just transitioning off the main sequence onto the subgiant branch, as suggested by our measured $\log g = 3.987^{+0.030}_{-0.036}$ dex (cm s^{-2}) and corresponding tight age constraint within our global fit from the MIST evolutionary tracks of $1.99^{+0.55}_{-0.40}$ Gyr. It hosts a planetary companion, TOI-640 b, which is a highly inflated ($R_{\rm P} = 1.771^{+0.060}_{-0.056}\ R_{\rm J}$), Jupiter-mass ($M_{\rm P} = 0.88 \pm 0.16\ M_{\rm J}$) planet with a near-integer orbital period of 5.0037775 ± 0.0000048 days. The orbit of the planet is consistent with circular, $e = 0.050^{+0.054}_{-0.035}$. It is only the third hot Jupiter known with a highly inflated radius ($R_{\rm P} > 1.7$) and on a period >5 days, joining KELT-12 b (Stevens et al. 2017) and Kepler-435 b (Almenara et al. 2015). Interestingly, TOI-640 b is almost a twin of KELT-12 b, in that they are highly inflated Jupiter-mass planets on ~5 day orbits around similar subgiant host stars. All three host stars in this regime are evolved, possibly suggesting that the inflation is a result of the host star's recent evolution (Assef et al. 2009; Spiegel & Madhusudhan 2012; Hartman & Bakos 2016; Lopez & Fortney 2016). Similar to KELT-12b and Kepler-435 b, we see no evidence of any significant eccentricity.

4.3. TOI-1333 b

TOI-1333 (TIC 395171208) is a bright ($V = 9.49$), evolved F-star with a mass of $M_* = 1.464^{+0.076}_{-0.079}\ M_\odot$ and radius of $R_* = 1.925^{+0.064}_{-0.063}\ R_\odot$. The star appears to be slightly evolved, as suggested by its $\log g$ of $4.034^{+0.032}_{-0.033}$ dex (cm s^{-2}). As a result of its evolutionary stage, we estimate a relatively tight age constraint from the MIST evolutionary tracks of $2.33^{+0.71}_{-0.56}$ Gyr. Orbiting on a 4.720219 ± 0.000011 day period, the planetary companion TOI-1333 b has a radius of $1.396^{+0.056}_{-0.054}\ R_{\rm J}$, a mass of $M_{\rm P} = 2.37 \pm 0.24\ M_{\rm J}$, and an eccentricity that is consistent with circular ($e = 0.073^{+0.092}_{-0.052}$). This is not surprising given that our derived circularization timescale, $1.29^{+0.37}_{-0.33}$ Gyr, is similar to the age of the system.

In the case of TOI-1333, we have measured a periodicity of ~5.3 days from the ground-based and TESS photometry (we note that WASP identified a period 3× this). We have also measured a

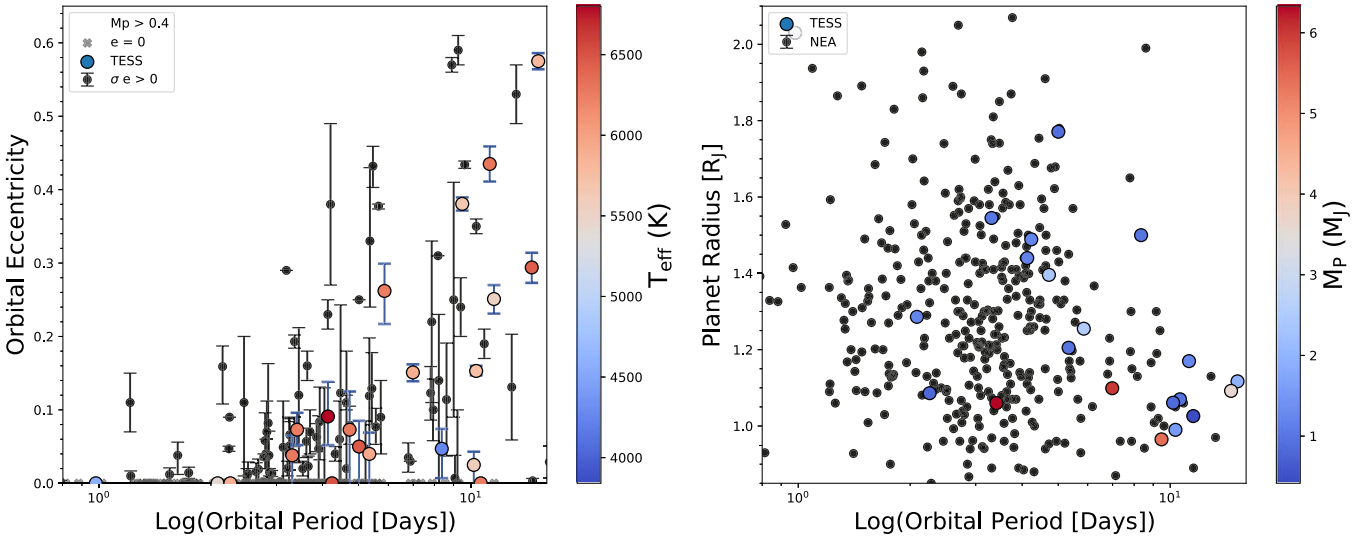

Figure 7. Left: eccentricity and log of the orbital period of all known giant planets with a mass greater than 0.4 M_J with period between 0.8 and 16 days. The TESS-discovered systems are colored by the host star's effective temperature. The systems with a measured eccentricity from the NASA Exoplanet Archive (NEA) are shown as black circles with errors. Systems where the eccentricity was assumed to be zero are shown with gray crosses. Right: radius and log of the orbital period of all known transiting giant planets. The systems known prior to TESS are in black, while the systems discovered by TESS, including those presented in this paper and Ikwut-Ukwa et al. (2021), are shown as circles colored by their planet's mass.

$v \sin I_*$ of 16.5 ± 0.5 km s^{-1}. If the periodicity identified in the photometry indeed is the average rotation period of the host star, then we can estimate the inclination of the host star's rotation axis and compare it to the derived inclination of TOI-1333 b's orbit following the methodology presented in Masuda & Winn (2020). Using the EXOFASTv2 implementation of a Markov Chain Monte Carlo, we run a simple fit of the host star's rotational velocity and its projection onto our line of sight ($v \sin I_*$) using the values from our global fit for Rstar ($1.925^{+0.064}_{-0.063}$ $R_\odot$), the derived rotational period of TOI-1333 from TESS and KELT (5.3 days), and the $v \sin I_*$ from the TRES spectroscopy (14.2 ± 0.5 km s^{-1}) to calculate the inclination of TOI-1333's rotation axis (relative to our line of sight). The latitudes on the Sun that show starspots have a differential rotation on the surface of a few percent. Therefore, we place a 3% error on the rotational velocity for this analysis. We require the same Gelman–Rubin statistic (<1.01) and independent draw (>1000) for convergence as the default for EXOFASTv2. We derive the inclination of the rotation axis to be $51.^\circ3^{+3.5}_{-3.3}$. From our global fit, TOI-1333 b has an inclination of $85.^\circ70^{+1.3}_{-0.65}$, suggesting that the rotation axis of the star and the orbital plane are misaligned. TOI-1333 b is an excellent candidate to confirm this result through spin–orbit alignment (λ) measurements using the Rossiter–McLaughlin or Doppler tomography techniques. The planet's orbit is also misaligned with the orbit of the wide binary companion TOI-1333 B, for which we measured an inclination of 125^{+18}_{-10} degrees from our LOFTI analysis. Interestingly, we do not detect a significant orbital eccentricity from our global fit for TOI-1333 b (though a small eccentricity is still possible), but this suggested misalignment might be a remnant left over from high-eccentricity migration. The likely bound companion at 470 au (see Section 2.6.2) could be responsible for Kozai–Lidov migration of the planet.

4.4. TOI-1478 b

TOI-1478 (TIC 409794137, $V = 10.81$) is a Sun-like G-dwarf with radius of $R_* = 1.048^{+0.030}_{-0.029}$ $R_\odot$, mass of $M_* = 0.946^{+0.059}_{-0.041}$ $M_\odot$, and an age of $9.2^{+3.1}_{-3.9}$ Gyr. Orbiting TOI-1478 is a warm Jupiter with a period of 10.180249 ± 0.000015 days, a radius of $R_P = 1.060^{+0.040}_{-0.039}$ R_J, and a mass of $M_P = 0.851^{+0.052}_{-0.047}$ M_J, and it resides in a circular orbit ($e = 0.024^{+0.032}_{-0.017}$). TOI-1478 b is the longest-period planet in our sample, and the planet and its host star (other than their orbital distances) resemble the Sun and Jupiter in mass and radius, possibly an example of an alternate outcome of our own solar system. As a result of the long orbital period, the tidal forces on TOI-1478 b are too weak to have circularized the orbit. Therefore, the lack of a significant eccentricity could suggest a more dynamically quiescent migration history.

4.5. TOI-1601 b

In the case of TOI-1601 b, our global model showed a clear bimodality in the posterior distribution of the host star's mass and age (see Section 3.1). This is likely due to the host star's evolutionary status, because the star sits on the Hertzprung–Russell diagram where isochrones cross, so the evolutionary state is ambiguous given the precision of our observations. To account for this, we extract two separate solutions, one for each peak in our posteriors. The higher host star mass solution, $M_* = 1.517^{+0.053}_{-0.049}$ $M_\odot$, has a higher probability of being correct at 66.7%, so we adopt this solution for the discussion, but both results are available in Table 4. TOI-1601 (TIC 139375960, $V = 10.71$) is an evolved subgiant ($\log g$ of $3.940^{+0.022}_{-0.025}$ dex (cm s^{-2})) with a radius of $R_* = 2.186^{+0.074}_{-0.063}$ $R_\odot$. We estimate the age of the system within our fit to be $2.64^{+0.38}_{-0.39}$ Gyr. TOI-1601 b is a Jupiter-mass planet (0.99 ± 0.11 M_J) that shows some inflation ($R_P = 1.159^{+0.062}_{-0.059}$ R_J) and a circular orbit ($e = 0.037^{+0.045}_{-0.026}$), and a 5.331752 ± 0.000011 day orbit. The spectroscopic analysis of the TRES spectra of TOI-1601 shows some metal enhancement ([Fe/H] $= 0.316^{+0.072}_{-0.074}$).

4.6. TESS's Impact on Giant Planets

While the primary goal of NASA's TESS mission is to discover and measure the masses of small planets (Ricker et al. 2015), TESS has already provided some valuable discoveries in

the field of giant planets (see, e.g., Armstrong et al. 2020; Huang et al. 2020a; Vanderburg et al. 2020). Given the minimum ~27 day baseline for any target and the completeness in the sensitivity of space-based photometry to detect a hot-Jupiter transit, TESS provides the opportunity to obtain a near-complete sample of hot Jupiters (Zhou et al. 2019). To date, TESS has discovered 26 giant planets ($M_P > 0.4\ M_J$), 16 of which have an orbital period >5.0 days (these numbers include the five systems presented in this paper and two additional systems from Ikwut-Ukwa et al. 2021). For comparison, 36 hot Jupiters have been discovered with orbital periods >5.0 days from ground-based transit surveys (NASA Exoplanet Archive, Akeson et al. 2013).

If giant planets predominantly migrate through dynamical interactions, we may find evidence of this evolutionary history in the eccentricity distribution of hot Jupiters, specifically those that are dynamically young (where the circularization timescale by tidal forces is longer than the age of the system). Figure 7 shows the current distribution of giant planet eccentricities as a function of orbital period out to 16 days. Those 26 systems discovered by TESS are shown colored by their host star's effective temperature. Although this is not a homogeneous sample, since a variety of different analysis methods and assumptions were made within this population, there is a wider distribution of eccentricities for those systems with an orbital period >5 days, where tidal circularization timescales are longer (Adams & Laughlin 2006). Interestingly, of the five systems presented here, only TOI-628 b has a statistically significant measured eccentricity ($e = 0.072^{+0.021}_{-0.023}$) and is consistent with dynamically driven migration since its estimated age is less than the circularization timescale of the orbit. Although the other systems show some nonzero eccentricities from our global fits, they are not statistically significant (>3σ) and could be a result of the Lucy–Sweeney bias (Lucy & Sweeney 1971). We also note that there is one very massive hot Jupiter in our sample, TOI-628 b (M_P $6.33^{+0.29}_{-0.31}\ M_J$), and it is the most massive hot Jupiter discovered to date by TESS (we note that TESS has discovered a few transiting brown dwarfs; Jackman et al. 2019; Carmichael et al. 2020, 2021; Šubjak et al. 2020; and WD 1856+534, which has a mass limit <13.8 M_J, Vanderburg et al. 2020). These massive Jupiters provide a great laboratory for studying the effect of high gravity on the atmosphere of a gas giant, while studying the transition point between giant planets and brown dwarfs.

5. Conclusion

We present the discovery and characterization of five new giant planets (TOI-628, TOI-640 b, TOI-1333 b, TOI-1478 b, and TOI-1601 b) from NASA's TESS mission. These planets were discovered in the primary mission using the 30 minute cadence, full-frame images. Of the systems, TOI-640 b, TOI-1333 b, and TOI-1601 b all orbit stars that appear to have just evolved off the main sequence and are entering the subgiant phase, as suggested by their estimated $\log g$ being under 4.1 dex (cm s^{-2}). None of the planets orbiting these subgiants appear to reside in significantly eccentric orbits. TOI-628 b is the most massive hot Jupiter discovered by TESS ($M_P = 6.33^{+0.29}_{-0.31}\ M_J$) and resides in an eccentric orbit that is consistent with dynamically driven migration. Another planet from this work, TOI-640 b, is one of the only highly inflated (>1.7 R_J) hot Jupiters with an orbital period greater than 5 days. TOI-1478 b is the only planet in this sample with an orbital period >10 days, and it and its star are similar in size and mass to Jupiter and the Sun. All five planets orbit bright ($V < 10.7$) host stars and significantly increase the sample of well-characterized, long-period (>5 day), hot Jupiters, an area where NASA's TESS mission should continue to provide a wealth of discoveries.

C.Z. is supported by a Dunlap Fellowship at the Dunlap Institute for Astronomy & Astrophysics, funded through an endowment established by the Dunlap family and the University of Toronto. T.H. acknowledges support from the European Research Council under the Horizon 2020 Framework Program via the ERC Advanced Grant Origins 83 24 28. J.V.S. acknowledges funding from the European Research Council (ERC) under the European Union's Horizon 2020 research and innovation program (project Four Aces; grant agreement No. 724427). P.R. acknowledges support from NSF grant No. 1952545. R.B. acknowledges support from FONDECYT Project 11200751 and from CORFO project No. 14ENI2-26865. A.J., R.B., and M.H. acknowledge support from project IC120009 "Millennium Institute of Astrophysics (MAS)" of the Millennium Science Initiative, Chilean Ministry of Economy. D.J.S. acknowledges funding support from the Eberly Research Fellowship from The Pennsylvania State University Eberly College of Science. The Center for Exoplanets and Habitable Worlds is supported by the Pennsylvania State University, the Eberly College of Science, and the Pennsylvania Space Grant Consortium. K.K.M. gratefully acknowledges support from the New York Community Trust's Fund for Astrophysical Research. L.G. and A.G. are supported by NASA Massachusetts Space Grant Fellowships. E.W.G., M.E., and P.C. acknowledge support by Deutsche Forschungsgemeinschaft (DFG) grant HA 3279/12-1 within the DFG Schwerpunkt SPP1992, Exploring the Diversity of Extrasolar Planets. B.S.G. was partially supported by the Thomas Jefferson Chair for Space Exploration at the Ohio State University. C.D. acknowledges support from the Hellman Fellows Fund and NASA XRP via grant 80NSSC20K0250.

We thank the CHIRON team members, including Todd Henry, Leonardo Paredes, Hodari James, Azmain Nisak, Rodrigo Hinojosa, Roberto Aviles, Wei-Chun Jao, and CTIO staffs, for their work in acquiring RVs with CHIRON at CTIO. This research has made use of SAO/NASA's Astrophysics Data System Bibliographic Services. This research has made use of the SIMBAD database, operated at CDS, Strasbourg, France. This work has made use of data from the European Space Agency (ESA) mission Gaia (https://www.cosmos.esa.int/gaia), processed by the Gaia Data Processing and Analysis Consortium (DPAC; https://www.cosmos.esa.int/web/gaia/dpac/consortium). Funding for the DPAC has been provided by national institutions, in particular the institutions participating in the Gaia Multilateral Agreement. This work makes use of observations from the LCO network. This work is based in part on observations obtained at the Southern Astrophysical Research (SOAR) telescope, which is a joint project of the Ministério da Ciência, Tecnologia e Inovações (MCTI/LNA) do Brasil, the U.S. National Science Foundation's NOIRLab, the University of North Carolina at Chapel Hill (UNC), and Michigan State University (MSU).

Funding for the TESS mission is provided by NASA's Science Mission directorate. We acknowledge the use of public TESS Alert data from pipelines at the TESS Science Office and at the TESS Science Processing Operations Center. This

research has made use of the NASA Exoplanet Archive and the Exoplanet Follow-up Observation Program website, which are operated by the California Institute of Technology, under contract with the National Aeronautics and Space Administration under the Exoplanet Exploration Program. This paper includes data collected by the TESS mission, which are publicly available from the Mikulski Archive for Space Telescopes (MAST). This paper includes observations obtained under Gemini program GN-2018B-LP-101. Resources supporting this work were provided by the NASA High-End Computing (HEC) Program through the NASA Advanced Supercomputing (NAS) Division at Ames Research Center for the production of the SPOC data products. This publication makes use of The Data & Analysis Center for Exoplanets (DACE), which is a facility based at the University of Geneva (CH) dedicated to extrasolar planet data visualization, exchange, and analysis. DACE is a platform of the Swiss National Centre of Competence in Research (NCCR) PlanetS, federating the Swiss expertise in exoplanet research. The DACE platform is available at https://dace.unige.ch.

Some of the data presented herein were obtained at the W. M. Keck Observatory, which is operated as a scientific partnership among the California Institute of Technology, the University of California, and the National Aeronautics and Space Administration. The Observatory was made possible by the generous financial support of the W. M. Keck Foundation. The authors wish to recognize and acknowledge the very significant cultural role and reverence that the summit of Maunakea has always had within the indigenous Hawaiian community. We are most fortunate to have the opportunity to conduct observations from this mountain.

MINERVA-Australis is supported by Australian Research Council LIEF Grant LE160100001, Discovery Grant DP180100972, Mount Cuba Astronomical Foundation, and institutional partners University of Southern Queensland, UNSW Sydney, MIT, Nanjing University, George Mason University, University of Louisville, University of California Riverside, University of Florida, and The University of Texas at Austin. We respectfully acknowledge the traditional custodians of all lands throughout Australia, and recognize their continued cultural and spiritual connection to the land, waterways, cosmos, and community. We pay our deepest respects to all Elders, ancestors and descendants of the Giabal, Jarowair, and Kambuwal nations, upon whose lands the MINERVA-Australis facility at Mt. Kent is situated.

Facilities: TESS, FLWO 1.5 m (Tillinghast Reflector Echelle Spectrograph), 4.1 m Southern Astrophysical Research (SOAR), LCO 0.4 m, LCO 1.0 m, 2.2 m telescope La Silla (Fiber-fed Extended Range Optical Spectrograph), KECK (NIRC2), PALOMAR (PHARO), TESS, KELT, WASP, CTIO 1.5 m (CHIRON), MINERVA-Australis, GEMINI (NIRI).

Software: EXOFASTv2 (Eastman et al. 2013, 2019), AstroImageJ (Collins et al. 2017), TAPIR (Jensen 2013), PEST Pipeline (http://pestobservatory.com/the-pest-pipeline/), LOFTI (Pearce et al. 2020), Isochrones package (Morton 2015), QLP Pipeline (Huang et al. 2020b), CETES (Brahm et al. 2017).

ORCID iDs

Joseph E. Rodriguez https://orcid.org/0000-0001-8812-0565
Samuel N. Quinn https://orcid.org/0000-0002-8964-8377
George Zhou https://orcid.org/0000-0002-4891-3517
Andrew Vanderburg https://orcid.org/0000-0001-7246-5438
Louise D. Nielsen https://orcid.org/0000-0002-5254-2499
Robert A. Wittenmyer https://orcid.org/0000-0001-9957-9304
Rafael Brahm https://orcid.org/0000-0002-9158-7315
Phillip A. Reed https://orcid.org/0000-0002-5005-1215
Chelsea X. Huang https://orcid.org/0000-0003-0918-7484
David R. Ciardi https://orcid.org/0000-0002-5741-3047
Ryan J. Oelkers https://orcid.org/0000-0002-0582-1751
Keivan G. Stassun https://orcid.org/0000-0002-3481-9052
Coel Hellier https://orcid.org/0000-0002-3439-1439
B. Scott Gaudi https://orcid.org/0000-0003-0395-9869
Jason D. Eastman https://orcid.org/0000-0003-3773-5142
Karen A. Collins https://orcid.org/0000-0001-6588-9574
Allyson Bieryla https://orcid.org/0000-0001-6637-5401
David W. Latham https://orcid.org/0000-0001-9911-7388
Ilaria Carleo https://orcid.org/0000-0002-0810-3747
Duncan J. Wright https://orcid.org/0000-0001-7294-5386
Elisabeth Matthews https://orcid.org/0000-0003-0593-1560
Erica J. Gonzales https://orcid.org/0000-0002-9329-2190
Carl Ziegler https://orcid.org/0000-0002-0619-7639
Courtney D. Dressing https://orcid.org/0000-0001-8189-0233
Steve B. Howell https://orcid.org/0000-0002-2532-2853
Thiam-Guan Tan https://orcid.org/0000-0001-5603-6895
Peter Plavchan https://orcid.org/0000-0002-8864-1667
Kim K. McLeod https://orcid.org/0000-0001-9504-1486
David Baker https://orcid.org/0000-0002-2970-0532
Gavin Wang https://orcid.org/0000-0003-3092-4418
Don J. Radford https://orcid.org/0000-0002-3940-2360
Richard P. Schwarz https://orcid.org/0000-0001-8227-1020
George R. Ricker https://orcid.org/0000-0003-2058-6662
Roland K. Vanderspek https://orcid.org/0000-0001-6763-6562
Sara Seager https://orcid.org/0000-0002-6892-6948
Joshua N. Winn https://orcid.org/0000-0002-4265-047X
Jon M. Jenkins https://orcid.org/0000-0002-4715-9460
Brett Addison https://orcid.org/0000-0003-3216-0626
D. R. Anderson https://orcid.org/0000-0001-7416-7522
Thomas Barclay https://orcid.org/0000-0001-7139-2724
Thomas G. Beatty https://orcid.org/0000-0002-9539-4203
Francois Bouchy https://orcid.org/0000-0002-7613-393X
Brendan P. Bowler https://orcid.org/0000-0003-2649-2288
C. E. Brasseur https://orcid.org/0000-0002-9314-960X
César Briceño https://orcid.org/0000-0001-7124-4094
Douglas A. Caldwell https://orcid.org/0000-0003-1963-9616
Michael L. Calkins https://orcid.org/0000-0002-2830-5661
Guillaume Chaverot https://orcid.org/0000-0003-4711-3099
Jessie L. Christiansen https://orcid.org/0000-0002-8035-4778
Kevin I. Collins https://orcid.org/0000-0003-2781-3207
Néstor Espinoza https://orcid.org/0000-0001-9513-1449
Gilbert A. Esquerdo https://orcid.org/0000-0002-9789-5474
Dax L. Feliz https://orcid.org/0000-0002-2457-7889
William Fong https://orcid.org/0000-0003-0241-2757
Tianjun Gan https://orcid.org/0000-0002-4503-9705
Steven Giacalone https://orcid.org/0000-0002-8965-3969

Holden Gill https://orcid.org/0000-0001-6171-7951
Lindsey Gordon https://orcid.org/0000-0002-8651-7611
A. Granados https://orcid.org/0000-0003-2099-9096
Nolan Grieves https://orcid.org/0000-0001-8105-0373
Natalia Guerrero https://orcid.org/0000-0002-5169-9427
Thomas Henning https://orcid.org/0000-0002-1493-300X
Katharine Hesse https://orcid.org/0000-0002-2135-9018
Melissa J. Hobson https://orcid.org/0000-0002-5945-7975
Jonathan Horner https://orcid.org/0000-0002-1160-7970
David J. James https://orcid.org/0000-0001-5160-4486
Eric L. N. Jensen https://orcid.org/0000-0002-4625-7333
Mary Jimenez https://orcid.org/0000-0002-5000-9316
Andrés Jordán https://orcid.org/0000-0002-5389-3944
Stephen R. Kane https://orcid.org/0000-0002-7084-0529
John Kielkopf https://orcid.org/0000-0003-0497-2651
Rudolf B. Kuhn https://orcid.org/0000-0002-4236-9020
Natasha Latouf https://orcid.org/0000-0001-8079-1882
Nicholas M. Law https://orcid.org/0000-0001-9380-6457
Alan M. Levine https://orcid.org/0000-0001-8172-0453
Michael B. Lund https://orcid.org/0000-0003-2527-1598
Andrew W. Mann https://orcid.org/0000-0003-3654-1602
Shude Mao https://orcid.org/0000-0001-8317-2788
Rachel A. Matson https://orcid.org/0000-0001-7233-7508
Matthew W. Mengel https://orcid.org/0000-0002-7830-6822
Jessica Mink https://orcid.org/0000-0003-3594-1823
Jack Okumura https://orcid.org/0000-0002-4876-8540
Enric Palle https://orcid.org/0000-0003-0987-1593
Joshua Pepper https://orcid.org/0000-0002-3827-8417
Elisa V. Quintana https://orcid.org/0000-0003-1309-2904
Paula Sarkis https://orcid.org/0000-0001-8128-3126
Arjun B. Savel https://orcid.org/0000-0002-2454-768X
Joshua E. Schlieder https://orcid.org/0000-0001-5347-7062
Avi Shporer https://orcid.org/0000-0002-1836-3120
Ramotholo Sefako https://orcid.org/0000-0003-3904-6754
Julia V. Seidel https://orcid.org/0000-0002-7990-9596
Robert J. Siverd https://orcid.org/0000-0001-5016-3359
Daniel J. Stevens https://orcid.org/0000-0002-5951-8328
Caitlin Stibbards https://orcid.org/0000-0003-0091-3769
C. G. Tinney https://orcid.org/0000-0002-7595-0970
Daniel A. Yahalomi https://orcid.org/0000-0003-4755-584X
Hui Zhang https://orcid.org/0000-0003-3491-6394

References

Adams, F. C., & Laughlin, G. 2006, ApJ, 649, 1004
Addison, B., Wright, D. J., Wittenmyer, R. A., et al. 2019, PASP, 131, 115003
Addison, B. C., Wright, D. J., Nicholson, B. A., et al. 2021, MNRAS, 502, 3704
Akeson, R. L., Chen, X., Ciardi, D., et al. 2013, PASP, 125, 989
Almenara, J. M., Damiani, C., Bouchy, F., et al. 2015, A&A, 575, A71
Armstrong, D. J., Lopez, T. A., Adibekyan, V., et al. 2020, Natur, 583, 39
Assef, R. J., Gaudi, B. S., & Stanek, K. Z. 2009, ApJ, 701, 1616
Bakos, G. Á, Csubry, Z., Penev, K., et al. 2013, PASP, 125, 154
Barnes, S. I., Gibson, S., Nield, K., & Cochrane, D. 2012, Proc. SPIE, 8446, 844688
Batygin, K., Bodenheimer, P. H., & Laughlin, G. P. 2016, ApJ, 829, 114
Bensby, T., Feltzing, S., & Oey, M. S. 2014, A&A, 562, A71
Bensby, T., Oey, M. S., Feltzing, S., & Gustafsson, B. 2007, ApJL, 655, L89
Bovy, J. 2017, MNRAS, 470, 1360
Brahm, R., Espinoza, N., Jordán, A., et al. 2019, AJ, 158, 45
Brahm, R., Jordán, A., & Espinoza, N. 2017, PASP, 129, 034002
Brown, T. M., Baliber, N., Bianco, F. B., et al. 2013, PASP, 125, 1031
Buchhave, L. A., Bakos, G. Á, Hartman, J. D., et al. 2010, ApJ, 720, 1118
Buchhave, L. A., Latham, D. W., Johansen, A., et al. 2012, Natur, 486, 375
Burt, J. A., Nielsen, L. D., Quinn, S. N., et al. 2020, AJ, 160, 153
Carmichael, T. W., Quinn, S. N., Mustill, A. J., et al. 2020, AJ, 160, 53
Carmichael, T. W., Quinn, S. N., Zhou, G., et al. 2021, AJ, 161, 97
Choi, J., Dotter, A., Conroy, C., et al. 2016, ApJ, 823, 102
Ciardi, D. R., Beichman, C. A., Horch, E. P., & Howell, S. B. 2015, ApJ, 805, 16
Collier Cameron, A., Wilson, D. M., West, R. G., et al. 2007, MNRAS, 380, 1230
Collins, K. A., Kielkopf, J. F., Stassun, K. G., & Hessman, F. V. 2017, AJ, 153, 77
Coşkunoğlu, B., Ak, S., Bilir, S., et al. 2011, MNRAS, 412, 1237
Cutri, R. M., Skrutskie, M. F., van Dyk, S., et al. 2003, yCat, 2246, 0
D'Angelo, G., Kley, W., & Henning, T. 2003, ApJ, 586, 540
da Silva, R., Udry, S., Bouchy, F., et al. 2006, A&A, 446, 717
Dawson, R. I., & Johnson, J. A. 2018, ARA&A, 56, 175
Dekany, R., Roberts, J., Burruss, R., et al. 2013, ApJ, 776, 130
Demory, B.-O., & Seager, S. 2011, ApJS, 197, 12
Donati, J.-F., Semel, M., Carter, B. D., Rees, D. E., & Collier Cameron, A. 1997, MNRAS, 291, 658
Dotter, A. 2016, ApJS, 222, 8
Eastman, J., Gaudi, B. S., & Agol, E. 2013, PASP, 125, 83
Eastman, J. D., Rodriguez, J. E., Agol, E., et al. 2019, arXiv:1907.09480
Fabrycky, D., & Tremaine, S. 2007, ApJ, 669, 1298
Fűrész, G. 2008, PhD thesis, Univ. Szeged, Hungary
Furlan, E., Ciardi, D. R., Everett, M. E., et al. 2017, AJ, 153, 71
Gagné, J., Mamajek, E. E., Malo, L., et al. 2018, ApJ, 856, 23
Gaia Collaboration, Brown, A. G. A., Vallenari, A., et al. 2016, A&A, 595, A2
Gaia Collaboration, Brown, A. G. A., Vallenari, A., et al. 2018, A&A, 616, A1
Gaudi, B. S., Seager, S., & Mallen-Ornelas, G. 2005, ApJ, 623, 472
Goldreich, P., & Tremaine, S. 1980, ApJ, 241, 425
Gray, D. F. 2005, The Observation and Analysis of Stellar Photospheres (3rd ed.; Cambridge: Cambridge Univ. Press)
Grunblatt, S. K., Huber, D., Gaidos, E. J., et al. 2016, AJ, 152, 185
Guerrero, N. M., Seager, S., Huang, C. X., et al. 2021, ApJS, in press
Hartman, J. D., & Bakos, G. Á 2016, A&C, 17, 1
Hayward, T. L., Brandl, B., Pirger, B., et al. 2001, PASP, 113, 105
Henderson, C. B., & Stassun, K. G. 2012, ApJ, 747, 51
Hodapp, K. W., Jensen, J. B., Irwin, E. M., et al. 2003, PASP, 115, 1388
Høg, E., Fabricius, C., Makarov, V. V., et al. 2000, A&A, 355, L27
Howell, S. B., Everett, M. E., Sherry, W., Horch, E., & Ciardi, D. R. 2011, AJ, 142, 19
Huang, C. X., Burt, J., Vanderburg, A., et al. 2018, ApJL, 868, L39
Huang, C. X., Quinn, S. N., Vanderburg, A., et al. 2020a, ApJL, 892, L7
Huang, C. X., Vanderburg, A., Pál, A., et al. 2020b, RNAAS, 4, 206
Huber, D., Chaplin, W. J., Chontos, A., et al. 2019, AJ, 157, 245
Ikwut-Ukwa, M., Rodriguez, J. E., Quinn, S. N., et al. 2021, arXiv:2102.02222
Jackman, J. A. G., Wheatley, P. J., Bayliss, D., et al. 2019, MNRAS, 489, 5146
Jensen, E. 2013, Tapir: A Web Interface for Transit/eclipse Observability, Astrophysics Source Code Library, ascl:1306.007
Johnson, M. C., Cochran, W. D., Albrecht, S., et al. 2014, ApJ, 790, 30
Jones, M. I., Brahm, R., Espinoza, N., et al. 2019, A&A, 625, A16
Kaufer, A., Stahl, O., Tubbesing, S., et al. 1999, Msngr, 95, 8
Kossakowski, D., Espinoza, N., Brahm, R., et al. 2019, MNRAS, 490, 1094
Kovács, G., Bakos, G., & Noyes, R. W. 2005, MNRAS, 356, 557
Kozai, Y. 1962, AJ, 67, 579
Kuhn, R. B., Rodriguez, J. E., Collins, K. A., et al. 2016, MNRAS, 459, 4281
Kurucz, R. L. 1992, in IAU Symp. 149, The Stellar Populations of Galaxies, ed. B. Barbuy & A. Renzini (Dordrecht: Kluwer), 225
Lidov, M. L. 1962, P&SS, 9, 719
Lin, D. N. C., Bodenheimer, P., & Richardson, D. C. 1996, Natur, 380, 606
Lin, D. N. C., & Papaloizou, J. 1986, ApJ, 309, 846
Lindegren, L., Hernández, J., Bombrun, A., et al. 2018, A&A, 616, A2
Liu, X., Burrows, A., & Ibgui, L. 2008, ApJ, 687, 1191
Lomb, N. R. 1976, Ap&SS, 39, 447
Lopez, E. D., & Fortney, J. J. 2016, ApJ, 818, 4
Lucy, L. B., & Sweeney, M. A. 1971, AJ, 76, 544
Mackereth, J. T., & Bovy, J. 2018, PASP, 130, 114501
Masuda, K., & Winn, J. N. 2020, AJ, 159, 81
Maxted, P. F. L., Anderson, D. R., Collier Cameron, A., et al. 2011, PASP, 123, 547
McLaughlin, D. B. 1924, ApJ, 60, 22
Miller, G. R. M., Collier Cameron, A., Simpson, E. K., et al. 2010, A&A, 523, A52
Morton, T. D. 2015, isochrones: Stellar Model Grid Package, Astrophysics Source Code Library, ascl:1503.010

Mugrauer, M., & Michel, K.-U. 2020, AN, 341, 996
Nagasawa, M., & Ida, S. 2011, ApJ, 742, 72
Naoz, S. 2016, ARA&A, 54, 441
Nelson, B. E., Ford, E. B., & Rasio, F. A. 2017, AJ, 154, 106
Nielsen, L. D., Bouchy, F., Turner, O., et al. 2019, A&A, 623, A100
Oelkers, R. J., Rodriguez, J. E., Stassun, K. G., et al. 2018, AJ, 155, 39
Paxton, B., Bildsten, L., Dotter, A., et al. 2011, ApJS, 192, 3
Paxton, B., Cantiello, M., Arras, P., et al. 2013, ApJS, 208, 4
Paxton, B., Marchant, P., Schwab, J., et al. 2015, ApJS, 220, 15
Pearce, L. A., Kraus, A. L., Dupuy, T. J., et al. 2020, ApJ, 894, 115
Pecaut, M. J., & Mamajek, E. E. 2013, ApJS, 208, 9
Pepper, J., Kane, S. R., Rodriguez, J. E., et al. 2020, AJ, 159, 243
Pepper, J., Kuhn, R. B., Siverd, R., James, D., & Stassun, K. 2012, PASP, 124, 230
Pepper, J., Pogge, R. W., DePoy, D. L., et al. 2007, PASP, 119, 923
Pepper, J., Stassun, K. G., & Gaudi, B. S. 2018, in Handbooks of Exoplanets, ed. H. Deeg & J. Belmonte (Cham: Springer), 128
Pollacco, D. L., Skillen, I., Collier Cameron, A., et al. 2006, PASP, 118, 1407
Queloz, D., Mayor, M., Udry, S., et al. 2001, Msngr, 105, 1
Quinn, S. N., White, R. J., Latham, D. W., et al. 2012, ApJL, 756, L33
Rasio, F. A., & Ford, E. B. 1996, Sci, 274, 954
Ricker, G. R., Winn, J. N., Vanderspek, R., et al. 2015, JATIS, 1, 014003
Rodriguez, J. E., Quinn, S. N., Huang, C. X., et al. 2019, AJ, 157, 191
Rossiter, R. A. 1924, ApJ, 60, 15
Savel, A. B., Dressing, C. D., Hirsch, L. A., et al. 2020, AJ, 160, 287
Scargle, J. D. 1982, ApJ, 263, 835
Schlafly, E. F., & Finkbeiner, D. P. 2011, ApJ, 737, 103
Schlecker, M., Kossakowski, D., Brahm, R., et al. 2020, AJ, 160, 275
Schlegel, D. J., Finkbeiner, D. P., & Davis, M. 1998, ApJ, 500, 525
Schönrich, R., Binney, J., & Dehnen, W. 2010, MNRAS, 403, 1829
Service, M., Lu, J. R., Campbell, R., et al. 2016, PASP, 128, 095004
Sha, L., Huang, C. X., Shporer, A., et al. 2021, AJ, 161, 82
Shallue, C. J., & Vanderburg, A. 2018, AJ, 155, 94
Siverd, R. J., Beatty, T. G., Pepper, J., et al. 2012, ApJ, 761, 123
Spiegel, D. S., & Burrows, A. 2013, ApJ, 772, 76
Spiegel, D. S., & Madhusudhan, N. 2012, ApJ, 756, 132
Stassun, K. G., Mathieu, R. D., Mazeh, T., & Vrba, F. J. 1999, AJ, 117, 2941
Stassun, K. G., Oelkers, R. J., Paegert, M., et al. 2019, AJ, 158, 138
Stassun, K. G., Oelkers, R. J., Pepper, J., et al. 2018, AJ, 156, 102
Stassun, K. G., & Torres, G. 2016, AJ, 152, 180
Stevens, D. J., Collins, K. A., Gaudi, B. S., et al. 2017, AJ, 153, 178
Šubjak, J., Sharma, R., Carmichael, T. W., et al. 2020, AJ, 159, 151
Tokovinin, A. 2018, PASP, 130, 035002
Tokovinin, A., Fischer, D. A., Bonati, M., et al. 2013, PASP, 125, 1336
Torres, G., Bakos, G. Á, Kovács, G., et al. 2007, ApJL, 666, L121
Vanderburg, A., Huang, C. X., Rodriguez, J. E., et al. 2019, ApJL, 881, L19
Vanderburg, A., & Johnson, J. A. 2014, PASP, 126, 948
Vanderburg, A., Rappaport, S. A., Xu, S., et al. 2020, Natur, 585, 363
Wang, S., Jones, M., Shporer, A., et al. 2019, AJ, 157, 51
Wu, Y., & Lithwick, Y. 2011, ApJ, 735, 109
Wu, Y., & Murray, N. 2003, ApJ, 589, 605
Zacharias, N., Finch, C., & Frouard, J. 2017, yCat, 1340, 0
Zhou, G., Huang, C. X., Bakos, G. Á, et al. 2019, AJ, 158, 141
Zhou, G., Quinn, S. N., Irwin, J., et al. 2020, AJ, 161, 2
Zhou, G., Rodriguez, J. E., Collins, K. A., et al. 2016, AJ, 152, 136
Zhou, G., Rodriguez, J. E., Vanderburg, A., et al. 2018, AJ, 156, 93
Ziegler, C., Tokovinin, A., Briceño, C., et al. 2020, AJ, 159, 19
Zinn, J. C., Pinsonneault, M. H., Huber, D., et al. 2019, ApJ, 885, 166